Current Research in Neurobiology 5 (2023) 100113

Contents lists available at ScienceDirect

Current Research in Neurobiology

journal homepage: www.sciencedirect.com/journal/current-research-in-neurobiology

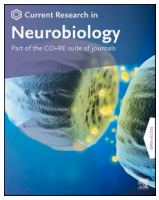

Apnea of prematurity induces short and long-term development-related transcriptional changes in the murine cerebellum

A. Rodriguez-Duboc [a], M. Basille-Dugay [b], A. Debonne [a,c], M.-A. Rivière [d], D. Vaudry [a,c], D. Burel [a,c,*]

[a] Univ Rouen Normandie, Inserm, U1245, Normandie Univ, F-76000, Rouen, France
[b] Univ Rouen Normandie, Inserm, U1239, Normandie Univ, F-76000, Rouen, France
[c] Univ Rouen Normandie, INSERM, CNRS, HeRacLeS US 51 UAR 2026, PRIMACEN, Normandie Univ, F-76000, Rouen, France
[d] Univ Rouen Normandie, UR 4108, LITIS Lab, INSA Rouen, NormaSTIC, CNRS 3638, Normandie Univ, F-76000, Rouen, France

ARTICLE INFO

Keywords:
Apnea of prematurity
Intermittent hypoxia
Transcriptome
Cerebellum
Development

ABSTRACT

Apnea of prematurity (AOP) affects more than 50% of preterm infants and leads to perinatal intermittent hypoxia (IH) which is a major cause of morbimortality worldwide. At birth, the human cerebellar cortex is still immature, making it vulnerable to perinatal events. Additionally, studies have shown a correlation between cerebellar functions and the deficits observed in children who have experienced AOP. Yet, the cerebellar alterations underpinning this link remain poorly understood. To gain insight into the involvement of the cerebellum in perinatal hypoxia-related consequences, we developed a mouse model of AOP. Our previous research has revealed that IH induces oxidative stress in the developing cerebellum, as evidenced by the over-expression of genes involved in reactive oxygen species production and the under-expression of genes encoding antioxidant enzymes. These changes suggest a failure of the defense system against oxidative stress and could be responsible for neuronal death in the cerebellum.

Building upon these findings, we conducted a transcriptomic study of the genes involved in the processes that occur during cerebellar development. Using real-time PCR, we analyzed the expression of these genes at different developmental stages and in various cell types. This enabled us to pinpoint a timeframe of vulnerability at P8, which represents the age with the highest number of downregulated genes in the cerebellum. Furthermore, we discovered that our IH protocol affects several molecular pathways, including proliferation, migration, and differentiation. This indicates that IH can impact the development of different cell types, potentially contributing to the histological and behavioral deficits observed in this model. Overall, our data strongly suggest that the cerebellum is highly sensitive to IH, and provide valuable insights into the cellular and molecular mechanisms underlying AOP. In the long term, these findings may contribute to the identification of novel therapeutic targets for improving the clinical management of this prevalent pathology.

1. Introduction

Apnea of prematurity (AOP) is particularly common in premature newborns due to their immature respiratory system (Moriette et al., 2010). This condition affects 50% of all preterm infants and nearly 100% of very preterm infants (i.e., born before 28 gestational weeks). AOP is characterized by breathing cessation episodes occurring at least every 5 min, and lasting over 20 s, which can be associated with bradycardia or O_2 desaturation (Eichenwald et al., 2016). AOP thus induces intermittent hypoxia (IH), which typically subsides in 98% of cases by the time the corrected term is reached. However, numerous studies have shown a correlation between the duration of AOP or the number of apneic events, and the occurrence of developmental abnormalities (Henderson-Smart, 1981; Janvier et al., 2004; Pergolizzi et al., 2022). The AOP-induced deficits include language, cognition, and motor impairments which can persist in the long term, and affect academic performance (Poets, 2020; Schmidt et al., 2017).

Due to its high metabolic requirements, the central nervous system

* Corresponding author. Univ Rouen Normandie, Inserm U1245, Normandie Univ, F-76000, Rouen, France.
E-mail addresses: agalic.rd@gmail.com (A. Rodriguez-Duboc), magalibasille@univ-rouen.fr (M. Basille-Dugay), aurelien.debonne1@univ-rouen.fr (A. Debonne), marc.aurele.riviere@gmail.com (M.-A. Rivière), david.vaudry@univ-rouen.fr (D. Vaudry), delphine.burel@univ-rouen.fr (D. Burel).

https://doi.org/10.1016/j.crneur.2023.100113
Received 2 August 2023; Received in revised form 22 September 2023; Accepted 9 October 2023
Available online 20 October 2023

(CNS) is particularly sensitive to O_2 availability, and the neurological consequences of a perinatal hypoxia are well documented. In humans, it has been demonstrated that perinatal hypoxia leads to region-specific cell death depending on the developmental stage. Specifically, in preterm infants, the periventricular white matter is most affected, while in term infants, the basal ganglia are the most vulnerable (Ferriero, 2001). Animal models have also revealed that other brain structures, such as the frontal cortex, corpus callosum, and brainstem, are targeted by perinatal hypoxia (Cai et al., 2012; Darnall et al., 2017; Kheirandish et al., 2005). However, the involvement of the cerebellum in perinatal hypoxia-related sequelae has been largely overlooked, despite the well-known vulnerability of the immature cerebellum to perinatal events in both humans and various animal models (Barron and Kim, 2020; Biran et al., 2011, 2012; Cai et al., 2012; Iskusnykh and Chizhikov, 2022). Furthermore, considering that several neurological functions known to be affected by perinatal hypoxia, such as learning and motor coordination, are partially controlled by the cerebellum (Volpe, 2009), these observations suggest that AOP could impact the neurological development of the cerebellum.

To study the effect of AOP on cerebellar development, we are using an animal hypoxia model, which involves exposing mice to 30 episodes of 120-s hypoxia for 6 h per day between P2 and P10 (Cai et al., 2012). It is now recognized that the first postnatal week in rodents (P0 to P10) corresponds, in terms of cerebellar cortical formation, to the third trimester of pregnancy in humans (24–38 weeks gestational age), which represents a period of infant prematurity and high vulnerability of the cerebellum (Biran et al., 2012; Volpe, 2009). Furthermore, it has been demonstrated that this protocol mimics the deficits caused by preterm apnea on myelination and axonal elongation in the brain (Cai et al., 2012). Thanks to this murine model of AOP, we have recently demonstrated that the cerebellum is indeed impacted by IH, leading to short- and long-term behavioral disorders, such as motor impairments and significant deficits in spatial learning (Leroux et al., 2022). These alterations are associated with a delay in cerebellar cortex differentiation, a density change in Purkinje cell arborization, a decrease of the volume of myelin sheaths, and an increase in afferent innervations (Cai et al., 2012; Leroux et al., 2022; Scheuer et al., 2017). However, the molecular mechanisms underlying IH-induced impairments have yet to be fully elucidated.

During episodes of hypoxia, O_2 deprivation is always followed by a reoxygenation phase (Prabhakar and Semenza, 2012). This causes both metabolic and oxidative stresses, which results in an increase of reactive oxygen species (ROS). Normally, cells can compensate for this increase by adjusting their energy metabolism and activating antioxidant mechanisms (Birben et al., 2012; Hardie et al., 2012). However, in the case of AOP, the chronic nature of IH leads to repeated reoxygenation phases. This cycle results in an over-production of ROS, which ends up surpassing the reducing capacity of antioxidant enzymes, causing oxidative stress (OS), and leading to neuronal defects (Cai et al., 2012; Leroux et al., 2022).

In this project, our aim was to determine whether there is a specific timeframe or cell type that is more vulnerable to IH during cerebellar development, and to uncover the molecular bases underlying short- and long-term deficits observed after AOP. We initially examined a specific panel of OS-related genes in the whole cerebellum at different postnatal stages, from P4 to adulthood. Subsequently, we performed a transcriptomic analysis of genes involved in different developmental processes such as proliferation, cell differentiation, and migration, on each cerebellar layer. As Purkinje cells represent the cerebellum's integration center and seem to be the most affected during AOP (Leroux et al., 2022), we also narrowed our focus to study these neurons. Altogether, our goal is to provide elements to correlate cerebellar transcriptomic regulations with both existing histological findings and long-term impairments observed in children having experienced AOP. Through these efforts, we aim to enhance our understanding of the cellular and molecular mechanisms underlying the pathophysiology of AOP.

2. Materials and methods

2.1. Animals

This study used wild type C57Bl6/J mice born and bred in an accredited animal facility (approval number B.76-451-04), in accordance with the French Ministry of Agriculture and the European Community Council Directive 2010/63/UE of September 22nd, 2010, on the protection of animals used for scientific purposes. The mice were kept under a 12-h light/dark cycle and had free access to food and water. Sex identification was done both by anogenital distance measurement and pigment-spot localization before sacrifice (Wolterink-Donselaar et al., 2009). Starting at P2, mice were assigned a unique identifier before initializing the protocol. There was no blinding in this study, and sample size was chosen based on power determination from our preliminary studies.

2.2. Intermittent hypoxia protocol

Our IH model relies on an in-house hypoxia chamber, which is based on the protocol developed by Cai et al. and has been validated to mimic AOP (Cai et al., 2012; Leroux et al., 2022). The IH sequence consisted of 2-min cycles of hypoxia (5% O2; 20 s/cycle) and reoxygenation, for 6 h per day, throughout the sleep phase of the animals (10 a.m. - 4 p.m.). Since it is now accepted that the first two postnatal weeks in mice correspond to a preterm period between 24 and 38 gestational weeks in humans, particularly in terms of cerebellum development (Biran et al., 2012; Haldipur et al., 2022), the protocol was initiated on neonatal P2 C57Bl6/J pups (IH group) and continued for a maximum of 10 consecutive days or until reaching the desired stage. During experiments, oxygen concentration, hygrometry, temperature, and atmospheric pressure were constantly monitored within the chamber. The control group (N) was placed in another chamber, which mimics the hypoxia chamber's environment, to control for external stressors.

2.3. Sample gathering

For real-time PCR experiments, mice were sacrificed at stages P4, P8, P12, P21, and P70 by decapitation after anesthesia by isoflurane inhalation (Iso-VET). Whole brains were immediately harvested and put in pure isopentane at −30 °C. They were then stored in sterile containers at −80 °C until further use. Sample size for real-time PCR were: 13 for P4 (7 N + 6IH), 16 for P8 (6 N + 10IH), 25 for P12 (15 N + 10IH), 17 for P21 (9 N + 8IH), and 8 for P70 (5 N + 3IH).

For immunohistochemistry, P8 mice were lethally anesthetized by intraperitoneal injection of ketamine (100 mg/kg) and xylazine (10 mg/kg), and then sacrificed by intracardiac perfusion of NaCl 9‰ and paraformaldehyde 4%, before removing the brains. Due to their diminutive size, brains from P4 mice were directly harvested and fixed by immersion. Brains were then submerged overnight in 4% paraformaldehyde, and then stored in phosphate buffer saline (PBS) prior to slicing. Sample size for IHC were: 13 for P4 (8 N + 5IH), and 12 for P8 (6 N + 6IH).

2.4. Panels and primer design

This project relies on 2 panels of genes of interest (GOI). The oxidative stress panel was developed by Lacaille et al. to specifically study OS, ROS increase mechanisms, and the cellular response to OS (Lacaille et al., 2015). Gene annotation, pathway identification and functions were investigated and illustrated with the Cytoscape software (v.3.9.1 (Shannon et al., 2003)) via STRING-DB (Szklarczyk et al., 2021) and ClueGO pathway annotations (v.2.5.9 (Bindea et al., 2009) (Fig. 1). The neurodevelopment panel was built based on the cerebellar development transcriptome database (CDT-DB; http://www.cdtdb.brain.riken.jp). This annotated experimental database includes layer-specific

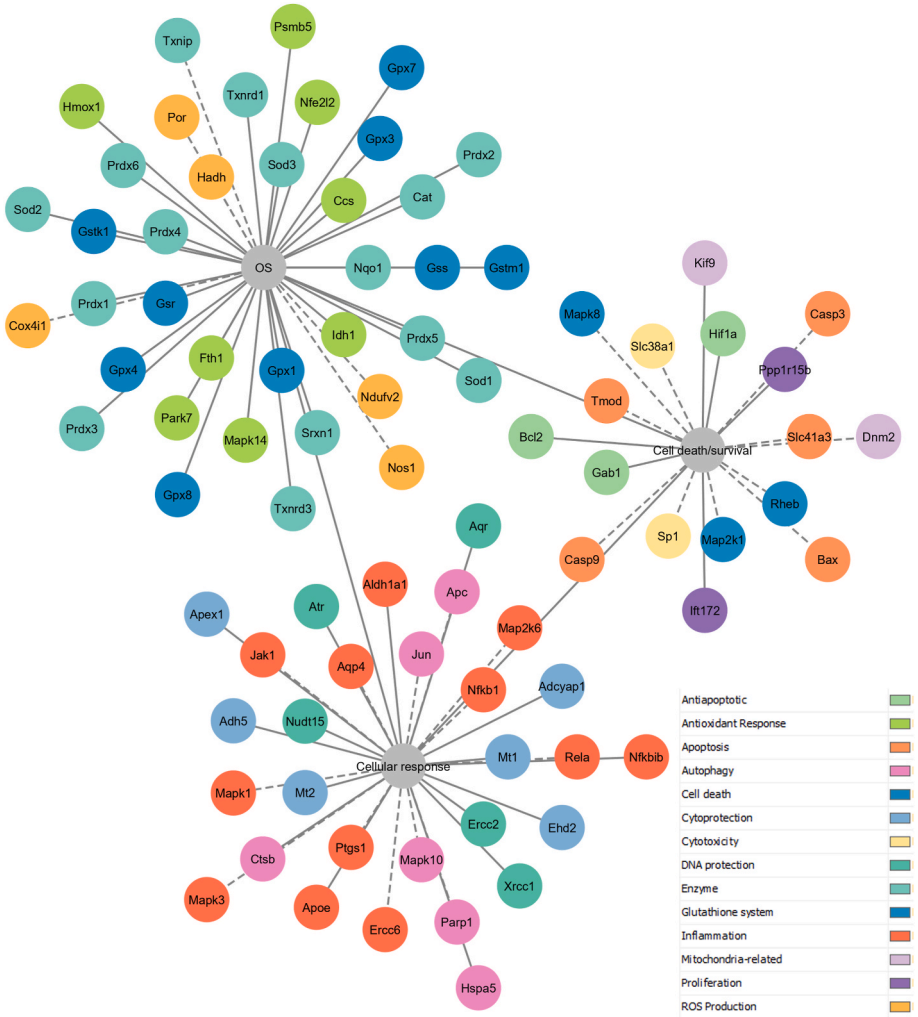

Fig. 1. Gene panel development: OS and its cellular effects. The gene set tested by real-time PCR was mapped in the Cytoscape software. Based on the literature, dashed lines represent genes with a deleterious effect if upregulated, while full lines represent genes with a beneficial effect if upregulated. Distinct colors indicate the pathways detailed in the following analysis. OS: oxidative stress. (For interpretation of the references to color in this figure legend, the reader is referred to the Web version of this article.)

genome-wide transcriptomic data for different developmental stages (Sato et al., 2008). In order to build this second panel, an analysis was conducted with the Cytoscape software (v.3.9.1 (Shannon et al., 2003)) using the expression data from the CDT-DB and protein interaction data retrieved from STRING-DB (Szklarczyk et al., 2021). The panel was further expanded by enrichment with the plugin stringApp (v 2.0.1; settings: maximum additional interactors = 10, confidence cutoff = 0.40 (Doncheva et al., 2019)) and then cross referenced with ClueGO pathway (v.2.5.9 (Bindea et al., 2009)) and functional data retrieved from the literature.

Gene primers were designed with the Primer Express software (v3.0.1; ThermoFischer Scientific) using nucleotide sequences from the NCBI Pubmed database. Primer pairs were supplied by Integrated DNA Technologies and validated by linear regression of serial dilution data. Primer pairs were chosen preferentially to be on exon joining sites, with the least possible hairpin and dimer formation, and with similar size, GC percentage, and melting temperature for forward and reverse primers. Each sequence was blasted on Pubmed to ensure specificity. See Appendices A and B for primer pair sequences and specifications.

2.5. Laser capture microdissection

Frozen brains were transferred to a −20 °C freezer 2 h prior to use. Brains were fixed to the refrigerated support (set to −20 °C) of the Cryomicrocut (Leica 3050) with Tissue-Tek by the frontal extremity. Cerebella were then cut into 14 µm-thick slices with a blade kept at −18 °C. Slices were immediately placed on membrane coated slides (cat. 415,190-9041-000 1.0 PEN, Carl Zeiss SAS) previously sterilized with dry heat (3 h at 170 °C). Each slide was stained with 2.8% cresyl violet solution and progressively dehydrated in ethanol solutions. For each cerebellar cortical layer (EGL, ML, IGL) and for the WM (excluding the deep cerebellar nuclei), a total surface of 700,000 µm^2 each was microdissected, while Purkinje cells were microdissected individually to amount to 130,000 µm^2 (for approximately 300 individual PCs). Each sample was processed with the LCM microscope and software (Leica; settings: zoom = x5 for layers/x20 for PCs, power = 50 for layers/30 for PCs, aperture = 12 for layers/17 for PCs, speed = 25 for layers/10 for PCs, specimen balance = 26, head current = 100%, pulse frequency = 120, offset = 110). The captured tissue was then kept in lysis buffer (LB1+LB2 from the Nucleospin RNA plus XS extraction kit by Macherey-Nagel) on ice until extraction.

2.6. RNA extraction

The samples issued from microdissection were purified on column using the Nucleospin RNA plus XS extraction kit from Macherey-Nagel

(cat. 740.990.250). The samples for whole cerebellum study were homogenized in 1 mL of Trizol (ThermoFisher), and mRNAs were further purified on column using the Nucleospin RNA extract II from Macherey-Nagel (cat. 740.955.250) according to manufacturer recommendations. RNA quantity and purity were analyzed by UV spectrophotometry (Nanodrop Technologies). The optical density (OD) of RNA was read at 230, 260, and 280 nm. The ratios OD 260 nm/OD 280 nm and OD 260 nm/DO 230 nm are calculated as indicators of protein, and salt/ethanol contamination, respectively. Ratio values between 1.6 and 2.0 were considered acceptable. As per the MIQE guidelines (Bustin et al., 2009), mRNA quality assessment was performed by a bioanalyser gel electrophoresis on RNA 6000 Pico chips (cat. 5067–1513, Agilent), and samples with an RNA integrity number (RIN) between 7 and 10 were considered qualitative enough to be analyzed. The mRNAs were then stored at −80 °C until the next step.

2.7. Real-time PCR

Total mRNAs were retrotranscribed to cDNA by reverse transcription using either *i)* the Quantitect RT Kit (cat. 205,313, Qiagen) for surfaces of 700,000 μm^2; *ii)* amplified and retrotranscribed with the SMARTer® Pico PCR cDNA Synthesis Kit and Advantage® 2 PCR Kit (cat. 634.928/7 and 639.207, Takara) for surfaces of 130,000 μm^2; or *iii*) retrotranscribed with the Prime Script RT reagent kit (cat. RR037A, Takara) for whole cerebella. The determination of the expression level of genes was done by real-time PCR in 384-well plates. The reaction volume was 5 μL including: 2.5 μL 2*X* Fast SYBR Green PCR Mastermix (cat. 4.385.612, Thermofisher), target gene-specific sense and antisense primers (0.15 μl of each, 100 nM final concentration), 1 μL PCR-grade water, and 1.2 μL of sample solution. The distribution of cDNA samples and reaction mixes was performed by the Bravo 1 liquid handling platform (Agilent). The real-time PCR reaction took place in a QuantStudio Flex 12 k thermal cycler (Applied Biosystems). For each gene of the panel, sample measurements were conducted at least in duplicate, with at least two housekeeping genes (HKG) from Table 1. Raw data output was calculated via the $2^{(-\Delta\Delta Cq)}$ method where:

$$2^{-\Delta\Delta Cq} = 2^{(-((CqGOI_{IH} - CqHKG_{IH}) - (CqGOI_N - CqHKG_N)))}$$

2.8. Immunohistochemistry

Fixed cerebella were cut coronally in 40 μm-thick slices with a vibratome (Leica Microsystems VT1000S), and then placed in a 24-well plate in 1 mL 1*X* PBS. Non-specific site blocking was first performed for 1 h in the presence of normal donkey serum diluted at 1:50 in an incubation solution containing 1*X* PBS, Triton X-100 (0.3%), and bovine serum albumin (1%). The slices were then incubated overnight at 4 °C with specific primary antibodies: i) rabbit cleaved caspase-3 (Cell signaling technology #9661 S at a 1:400 dilution) to mark apoptotic cells; or ii) mouse calbindin (Sigma Aldrich #C9848 at a 1:1000 dilution) to target Purkinje cells. Afterwards, the slices were rinsed with 1*X* PBS and incubated for 2 h at room temperature, with donkey anti-rabbit Alexa488 and donkey anti-mouse Alexa488 diluted at 1:300, respectively. This step was followed by 3 additional 1*X* PBS rinses. To visualize cerebellar layers, the slices were co-incubated with the nuclear marker 4′,6′-diamidino-2-phenylindole (DAPI; 1 μg/mL) for caspase 3 experiments or with donkey anti-rabbit Alexa568, which provided non-specific labeling of blood vessels under our experimental conditions. Following a final rinse, the sections were mounted on slides using Mowiol.

Coronal sections were chosen to acquire symmetrical images from as many lobules as possible. For each animal, 3 to 5 slices were selected in the whole cerebellum. For the area measurements and the counting of caspase-3-positive cells, images were acquired with a widefield microscope to reconstruct the whole slice (Thunder 3D, Leica). These data were analyzed with the Fiji software, version 1.53 (Schindelin et al., 2012). Each layer's surface area was outlined manually on Fiji based on DAPI marking. A pipeline was established for automated counting of cleaved caspase-3 spots by using the "analyze particles" Fiji tool (settings: circularity = 1, size = 30 to 100 μm^2). For each of these data, the total area of the slice was added to the statistical analysis to account for antero-posterior size variations. For Purkinje cell analysis at P8, image acquisition was completed on a confocal microscope (TCS SP8 MP, Leica Microsystems). Each image corresponds to a 10-μm thick section with 1-μm step z-stacks (2048 × 2048 focal planes) acquired using a × 40 objective. Analysis was done using the Imaris software (Andor Technology, Belfast, UK) and all three-dimensional reconstructions were done with the same threshold. The illustration in Fig. 8 corresponds to the optimal focus plane of the stacks.

2.9. Statistical analysis

Statistical analyses were performed within the R statistical computing environment (version 4.3). Both real-time PCR and IHC data were modeled through the Generalized Linear Mixed Model (GLMM) framework, using the {glmmTMB} package (Brooks et al., 2017).

For real-time PCR data, a Gaussian likelihood with an identity link function was used to model the distribution of the DCq samples for each gene of interest. When DCq samples for one gene were split over multiple plates, a random intercept was added to account for intra-plate correlations. Immunohistochemistry data consisted of many types of variables, which required different likelihood families. Count data (e.g., cell counts) were modeled using Generalized Poisson likelihoods, to account for potential over- or under-dispersion. Measures bound at 0 (e.g., cell density, areas, and volumes) were modeled using a Gamma likelihood, and proportions (e.g., ratios of areas) with a Beta likelihood. When multiple measures were taken from the same mouse, a mouse random intercept was added to account for the correlation between technical replicates (Zimmerman et al., 2021). For clarity, our plots display unit-level data (i.e., the value of a single slice from a single mouse) as semi-transparent dots, and mouse-averages (i.e., average of all slices' values belonging to a mouse) as diamonds.

Model diagnostics were done using the {DHARMa} (Hartig, 2022) and {performance} (Lüdecke et al., 2021) packages. The fitness of each

Table 1
Selected housekeeping genes for real-time **PCR experiments.**
Table providing, the list of housekeeping genes used, their full name and National Center for Biotechnology Information (NCBI) reference number. Primer sequences indicated were designed on the Primer Express software and ordered from Integrated DNA Technologies. Fw: forward; Rv: reverse.

Gene	Name	Function	NCBI reference	Primer pair sequence	
Gapdh	glyceraldehyde-3-phosphate dehydrogenase	glucose metabolism	NM_001289726.1	Forward	CATGGCCTTCCGTGTTCCTA
				Reverse	CCTGCTTCACCACCTTCTTGA
Hsp90ab1	heat shock protein 90 alpha (cytosolic), class B member 1	signal transduction	NM_008302.3	Forward	CAGAAATTGCCCAGCTCATGT
				Reverse	CCGTCAGGCTCTCATATCGAA
Ppia	peptidylprolyl isomerase A	protein folding	NM_008907.1	Forward	CCACTGTCGCTTTTCGCCGC
				Reverse	TGCAAACAGCTCGAAGGAGACGC
Ywhaz	tyrosine 3-monooxygenase/tryptophan 5-monooxygenase activation protein zeta	signal transduction	NM_011740.3	Forward	AGGACCTAAAAGGGTCGGTCA
				Reverse	CGGGGTTTCCTCCAATCACT

model was assessed through both visual checks (e.g., posterior predictive checks, QQ plots, residuals vs predicted values) and quantitative indices of model fit (e.g., AIC: Aikake Information Criterion). When several competing models were possible a priori, we selected the most plausible one primarily based on our theoretical understanding of the response's properties, and, to a lesser extent, to minimize AIC and favor model parsimony.

Contrasts and p-values for relevant hypotheses were obtained using the {emmeans} package (Lenth, 2022). They were computed on the link scale, using Wald t-tests, without any multiplicity adjustments. For all analyses, $p < .05$ was considered significant and for each figure asterisks indicate the level of statistical significance: one for $p < .05$, two for $p < .01$, and three for $p < .001$.

3. Results

In addition to the results mentioned below, all real-time PCR results are featured in Appendices C, D and E.

3.1. IH induces OS and triggers different cellular response mechanisms

1. All stages are sensitive to IH but P8 is more vulnerable

Among the 37 OS-related genes tested, 31 show differential expression between normoxia and IH at P4, P8, P12, P21, and/or P70 (Fig. 2). Cerebellar cells start responding to hypoxia at P4, with the maximum number of regulated genes observed at P12. However, this regulation is mainly a positive defense reaction with a high upregulation of antioxidant enzymes, such as Txnrd3 and Sod3. In contrast, the most deleterious regulation is found at P8, with the downregulation of 5 antioxidant enzymes (Txnrd1, Sod3, Prdx6, Prdx5 and Cat), and only a few beneficial regulations. After the end of the protocol, some genes remain differentially regulated or become so (Fig. 2). Two such genes are Idh1 and Txnrd3, which are upregulated at P12 and P21 but become downregulated at P70, or Ccs and Gpx 3 whose expression is only increased in adulthood.

2. IH induces the regulation of various cell death and survival pathways

Our immunohistochemical analysis indicated that the cleaved caspase-3 positive cells are mainly localized in the IGL and the WM (Fig. 3A). The comparison of the density of these cells between hypoxic and normoxic mice revealed a higher number of apoptotic cells after IH at P4 ($t(32) = -2.58$; $p = 0.015$; $Ratio = 0.454$; $CI_{95} = [0.243, 0.847]$) but no statistically significant difference between both conditions at P8

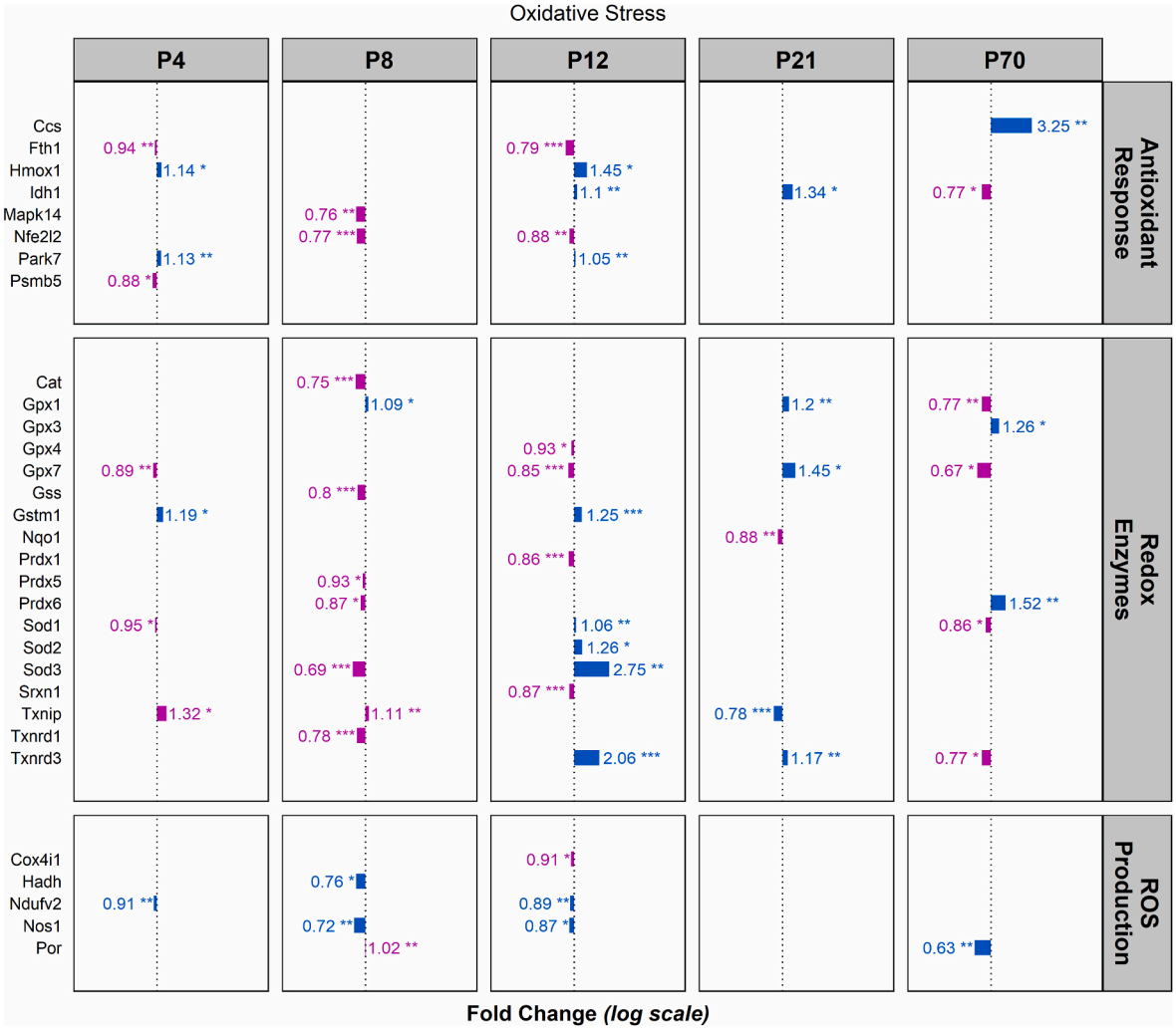

Fig. 2. All stages are sensitive to IH but P8 is more vulnerable. Significant real-time PCR results reflecting the regulation of the expression of genes involved in oxidative stress after IH in the whole cerebellum of P4, P8, P12, P21, and P70 mice. Deleterious effects (upregulation of pro-oxidative genes or downregulation of anti-oxidative genes) are represented in pink. Positive defense (upregulation of anti-oxidative genes or downregulation of pro-oxidative genes) are represented in blue. IH: intermittent hypoxia; Px: postnatal day x; ROS: reactive oxygen species. Asterisks indicate the level of statistical significance: one for $p < .05$, two for $p < .01$, and three for $p < .001$. (For interpretation of the references to color in this figure legend, the reader is referred to the Web version of this article.)

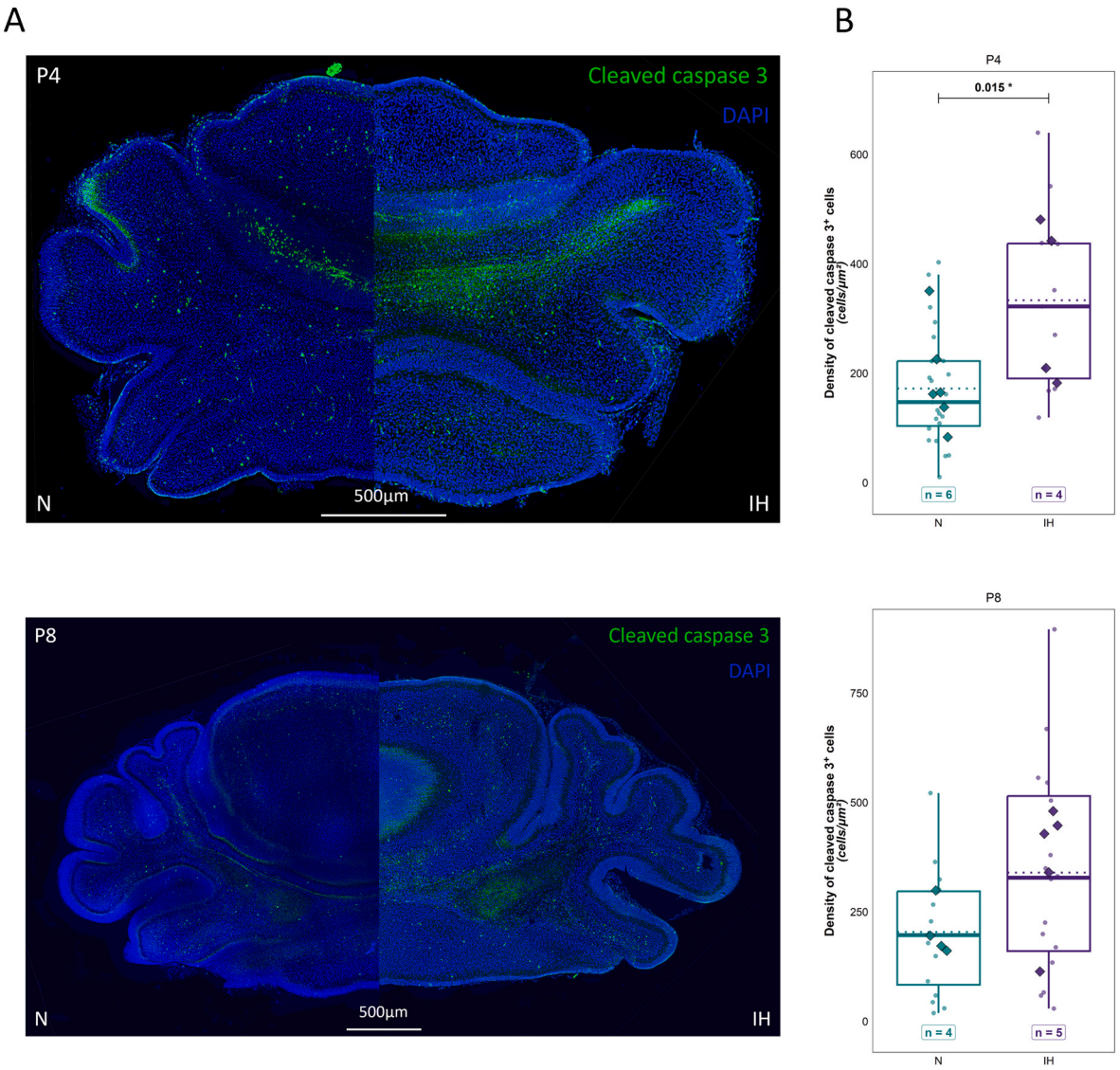

Fig. 3. IH induces an increase of caspase-3 apoptotic cells at P4 but not at later stages. A. Images illustrating the density of cleaved caspase-3 positive cells at P4 (upper image), P8 (bottom image)in the whole cerebellum of control (N; left side of image) or hypoxic (IH; right side of image). **B.** Density of cleaved caspase-3 positive cells at P4 (upper plot), P8 (bottom plot) in the whole cerebellum of control (N; left side) or hypoxic (IH; right side). Each slice analyzed is represented by a transparent dot, while mouse-averages of slices are represented by diamond shapes. The number of mice (n) present in each experimental group is indicated under each boxplot. IH: intermittent hypoxia; N: normoxia; Px: postnatal day x. Asterisks indicate the level of statistical significance: one for $p < .05$, two for $p < .01$, and three for $p < .001$.

($t(30) = -1.532$; $p = 0.136$; $Ratio = 0.591$; $CI_{95} = [0.293, 1.192]$) (Fig. 3B).

In contrast, real-time PCR results indicated that cell death/protection pathways are activated during IH. Indeed, after a slight regulation as early as P4, the response to IH is most prominent at P8 and P12, with 10 and 9 regulated genes, respectively. It is interesting to note that, at P8, there is a downregulation of genes expected to exert a protective effect on cellular components, such as the transcription factor Sp1. Meanwhile, there is an equilibrium between pro- and anti-apoptotic mechanisms at P8. However, the response is shifted towards an overall upregulation of the apoptotic pathway at P12 (Fig. 4), with the upregulation of both caspase-3 and -9 genes and downregulation of the anti-apoptotic gene Bcl2.

3. IH activates various cellular response pathways during cerebellar development

OS also triggers the activation of various cellular pathways, such as inflammation and autophagy. Indeed, 29 genes belonging to these intracellular pathways were tested on the whole cerebella of P4, P8, P12, P21, and P70 mice. 19 of these are differentially regulated by IH during cerebellar development (Fig. 4). At P4, IH induces a moderate pro-inflammatory (3 regulated genes) effect, while an opposite regulation is observed at P8, with 9 anti-inflammatory regulations. These expression modifications are somewhat maintained at P12, while Mt1 and Mt2 become markedly under-expressed at P21. Concerning autophagy and mitochondrial adaptation, the effect of IH is less clear since Kif9 and Hspa5, but also Jun and Parp1 are downregulated between P4 to P21. Finally, at P70, only a few genes are still dysregulated (Fig. 4).

3.2. The effect of IH on the cerebellum varies by stage and layer

A panel of 54 genes in total was tested in the different cerebellar layers, microdissected at P4, P8, P12, P21, and P70. A graphical representation provides an overview of the molecular pathways altered by IH, grouped by developmental stage and cerebellar layer (Fig. 5), and sorted

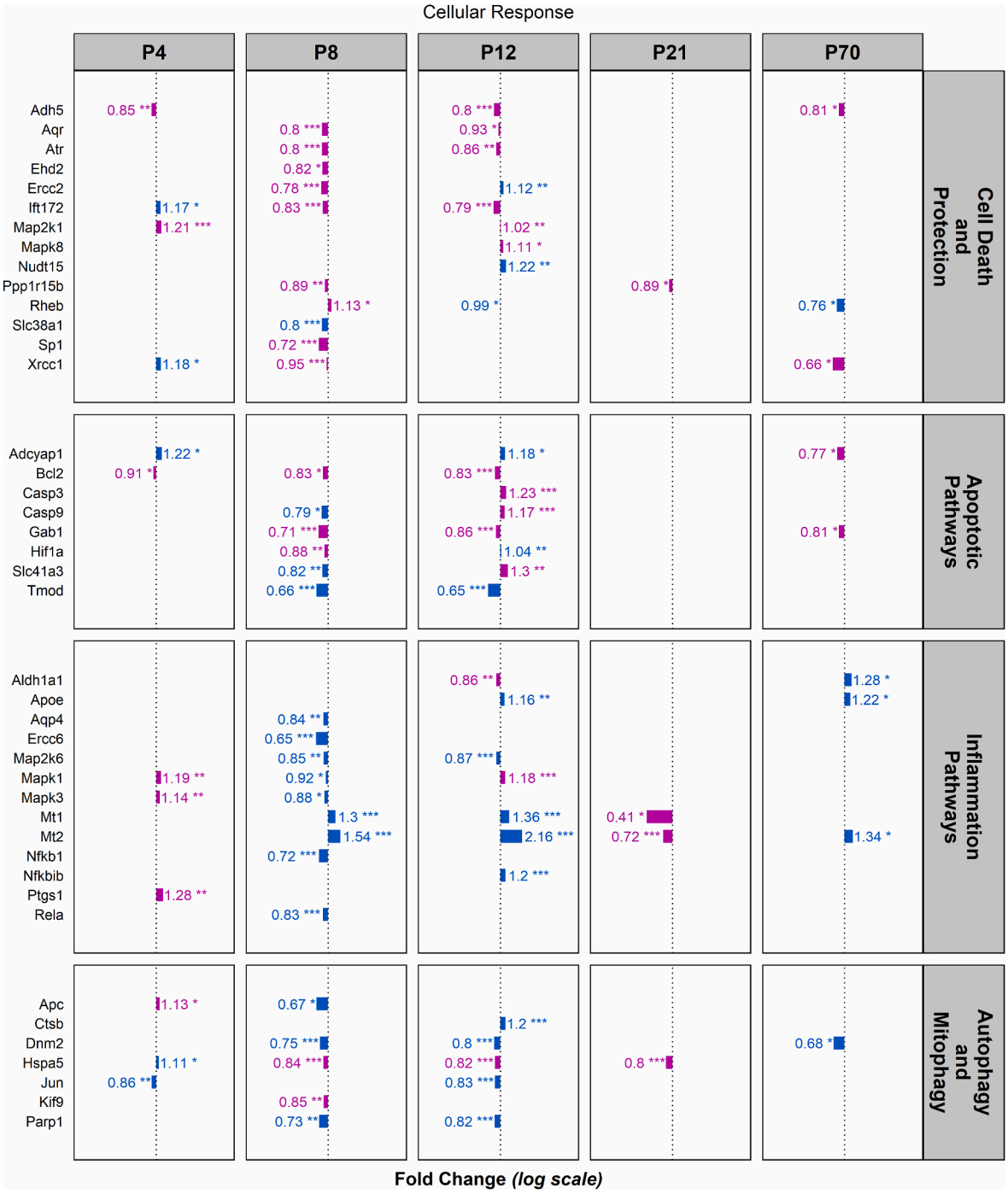

Fig. 4. IH activates various cellular response pathways during cerebellar development. Significant real-time PCR results reflecting the regulation of the expression of genes involved in the cellular response associated with oxidative stress in the whole cerebellum after IH in P4, P8, P12, P21, and P70 mice. Deleterious effects (upregulation of pro-oxidative genes or downregulation of anti-oxidative genes) are represented in pink. Positive defense (upregulation of anti-oxidative genes or downregulation of pro-oxidative genes) are represented in blue. IH: intermittent hypoxia; Px: postnatal day x. Asterisks indicate the level of statistical significance: one for $p < .05$, two for $p < .01$, and three for $p < .001$. (For interpretation of the references to color in this figure legend, the reader is referred to the Web version of this article.)

according to the major mechanisms implicated in cerebellar development i.e., proliferation and repair, cellular differentiation, migration and response, and cell communication. The impact of IH on each of these mechanisms is described below, but overall, the stage which presents the most transcriptomic regulations is P8 (Fig. 5).

1. IH affects the EGL and cellular proliferation

By using DAPI labelling, we have demonstrated that the area of the EGL is significantly smaller in IH mice at P4 ($t(32) = 2.903$; $p = 0.007$; $Ratio = 1.47$; $CI_{95} = [1.122, 1.927]$) but this difference is no longer present at P8 ($t(30) = 0.671$; $p = 0.507$; $Ratio = 1.083$; $CI_{95} = [0.85, 1.38]$) (Fig. 6A).

Of the 29 tested genes, 7 are regulated by IH at P4, 11 and 18, respectively, in the outer proliferative EGL and the inner premigratory EGL at P8, and 11 in the whole EGL at P12. Interestingly we mainly

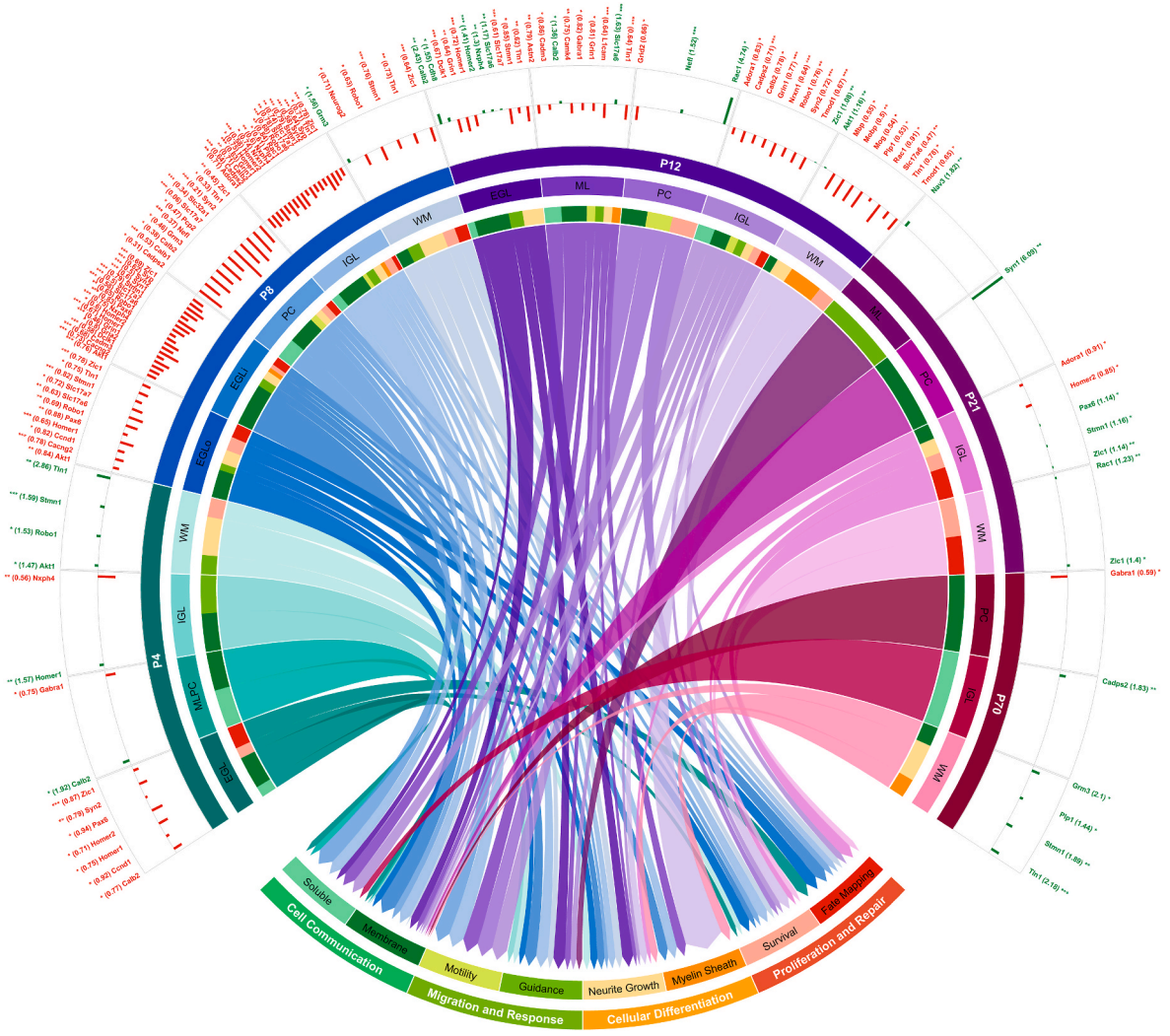

Fig. 5. Overview of the molecular pathways altered by IH grouped by stage and layer. Figure generated in R with the {Circlize} package (Gu et al., 2014) based on our results and pathway analysis. The upper two-thirds of the circumference represent each stage and the cerebellar layers microdissected in each. The lower third represents main pathways attributed to the genes tested. Connecting arrows indicate the overall regulation present in a layer by connecting it to the matching pathways. Likewise, the colors of each pathway are mirrored underneath each layer for readability. The significant real-time PCR results reflecting the regulation of the expression of genes involved in differentiation in each cerebellar layer are represented at the periphery of the circle as the fold change of hypoxic versus control mice at P4, P8, P12, P21, and P70. Upregulations are represented in green, and downregulations are represented in red. Results will be further detailed layer by layer in the following figures. EGL: external granular layer; EGLi: inner EGL; EGLo: outer EGL; IGL: internal granular layer; ML: molecular layer; PC: Purkinje cells; Px: postnatal day x; WM: white matter. Asterisks indicate the level of statistical significance: one for $p < .05$, two for $p < .01$, and three for $p < .001$. (For interpretation of the references to color in this figure legend, the reader is referred to the Web version of this article.)

observed an under-expression of these genes with the most significant effect of IH visible in the inner EGL at P8. Of note, cyclin Ccnd1 is downregulated at P4 and P8 in the proliferative outer EGL of IH mice, while the guidance-related gene Robo1 is downregulated in the whole EGL. In contrast, at P12, some genes specifically implicated in synapse formation, such as Calb2 and Homer2, or in migration, such as Cdh8, are upregulated (Fig. 6B).

2. IH alters neuronal migration and Purkinje cell development

No statistically significant difference in the area of the ML (including Purkinje cells) was found between IH and N mice at P4 ($t(32) = 0.113$; $p = 0.911$; $Ratio = 1.012$; $CI_{95} = [0.815, 1.257]$) nor P8 ($t(30) = 0.588$; $p = 0.561$; $Ratio = 1.051$; $CI_{95} = [0.884, 1.249]$) (Fig. 7A). At P4 and P8, the ML is too narrow to be microdissected, but the results obtained by testing 29 genes at P12 indicate that the IH protocol is associated with a downregulation of migration-associated genes, namely L1cam and Astn2, as well as some genes involved in cell differentiation or communication, such as Tln1 (talin 1), and Gabra1 or Grin1, respectively. At P21, only Nav3 is upregulated, and no gene expression modification is seen at P70 (Fig. 7B).

Focusing on PCs, we showed that their phenotype is not visibly altered by our IH protocol at P8 (Fig. 8A). Moreover, no significative difference has been observed in the density ($t(266) = 1.021$; $p = 0.308$; $Ratio = 1.049$; $CI_{\{95\}} = [0.957, 1.149]$) or in the volume ($t(266) = -0.05$; $p = 0.960$; $Ratio = 0.994$; $CI_{\{95\}} = [0.787, 1.256]$) of PCs between IH and N conditions (Fig. 8B). However, out of 33 OS-panel genes tested, 8 are downregulated at P8, notably the 6 antioxidant-coding genes Gpx4, Gsr and Prdx2, 3, 5, 6, (Fig. 8C). This phenomenon is accompanied by a decrease in the expression of the cytoskeletal proteins Tln1 and Nefl (neurofilament light polypeptide), and of the maturation-indicating genes Calb1, Slc17a7, and Syn2, including the Purkinje-specific gene Pcp2 (Fig. 8D). At P12, an equilibrium in positive and negative cell responses occurs with a downregulation of Gss and Prdx5, balanced by Parp1 and Rheb (Fig. 8C). In addition, Rac1, which is not affected by IH at P8, becomes upregulated at P12 (Fig. 8D), as well as

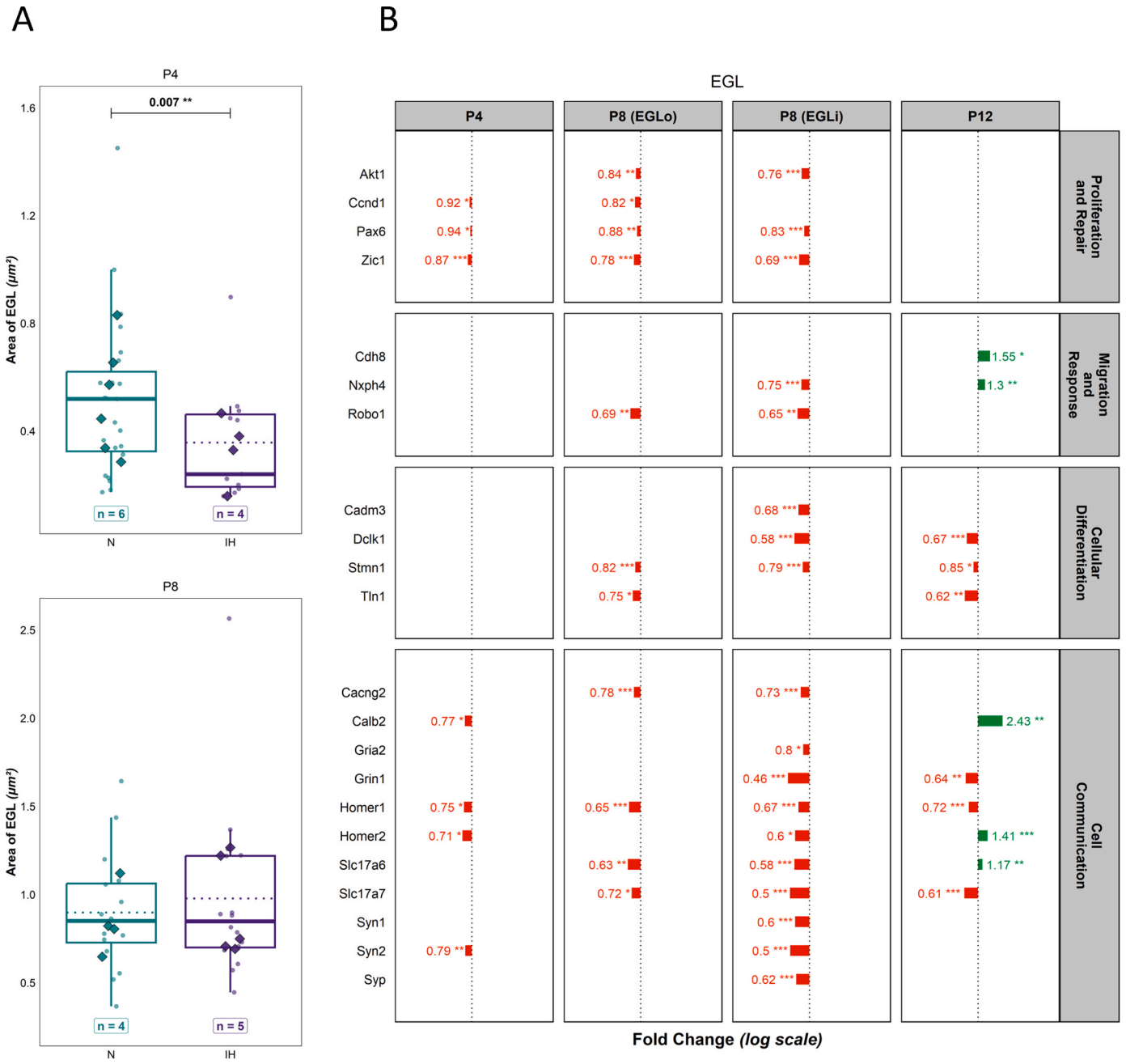

Fig. 6. Effect of IH on the EGL. A. Measurement of the area of the EGL in control (N) or hypoxic (IH) mice at P4 (upper plot), P8 (bottom plot). Each slice analyzed is represented by a transparent dot, while mouse-averages of slices are represented by diamond shapes. The number of mice (n) present in each experimental group is indicated under each boxplot. **B.** Significant real-time PCR results reflecting the IH-induced regulation of the expression of genes involved in EGL differentiation in P4, P8 and P12 mice. Upregulations are represented in green, and downregulations are represented in red. EGL: external granular layer; EGLi: inner EGL; EGLo: outer EGL; IH: intermittent hypoxia; N: normoxia; Px: postnatal day x. Asterisks indicate the level of statistical significance: one for $p < .05$, two for $p < .01$, and three for $p < .001$. (For interpretation of the references to color in this figure legend, the reader is referred to the Web version of this article.)

Calb and Slc17a6 in the ML (Fig. 7B). On the longer term (i.e., post-IH protocol), IH seems to modify the expression of only a few genes, such as Txrnd3, Gabra1, and Syn1 (Fig. 8C and D).

3. IH affects major differentiation processes in the IGL

A slight decrease in the area of IGL in IH mice was observed at P4 ($t(32) = 2.464$; $p = 0.019$; $Ratio = 1.176$; $CI_{95} = [1.029, 1.345]$), but this difference is no longer significant at P8 ($t(30) = -1.625$; $p = 0.115$; $Ratio = 0.915$; $CI_{95} = [0.819, 1.023]$) (Fig. 9A).

However, at P8, IH downregulates 18 genes out of the 30 tested, including 12 genes associated with synaptogenesis and neuronal maturation (Fig. 9B). Among them, we find Homer1/2, Syn2, and Syp. Interestingly, the cerebellum-specific Nrxn1 and/or its ligand Nxph4 are both downregulated during the whole IH protocol period. At P21, a mild upregulation of the cytoskeletal gene Stmn1 is observed, whereas it is previously found downregulated at P12. In contrast, the synapse-associated Cadps2 is downregulated at P8 and P12 but becomes upregulated at P70 (Fig. 9B).

4. Effect of IH on the WM

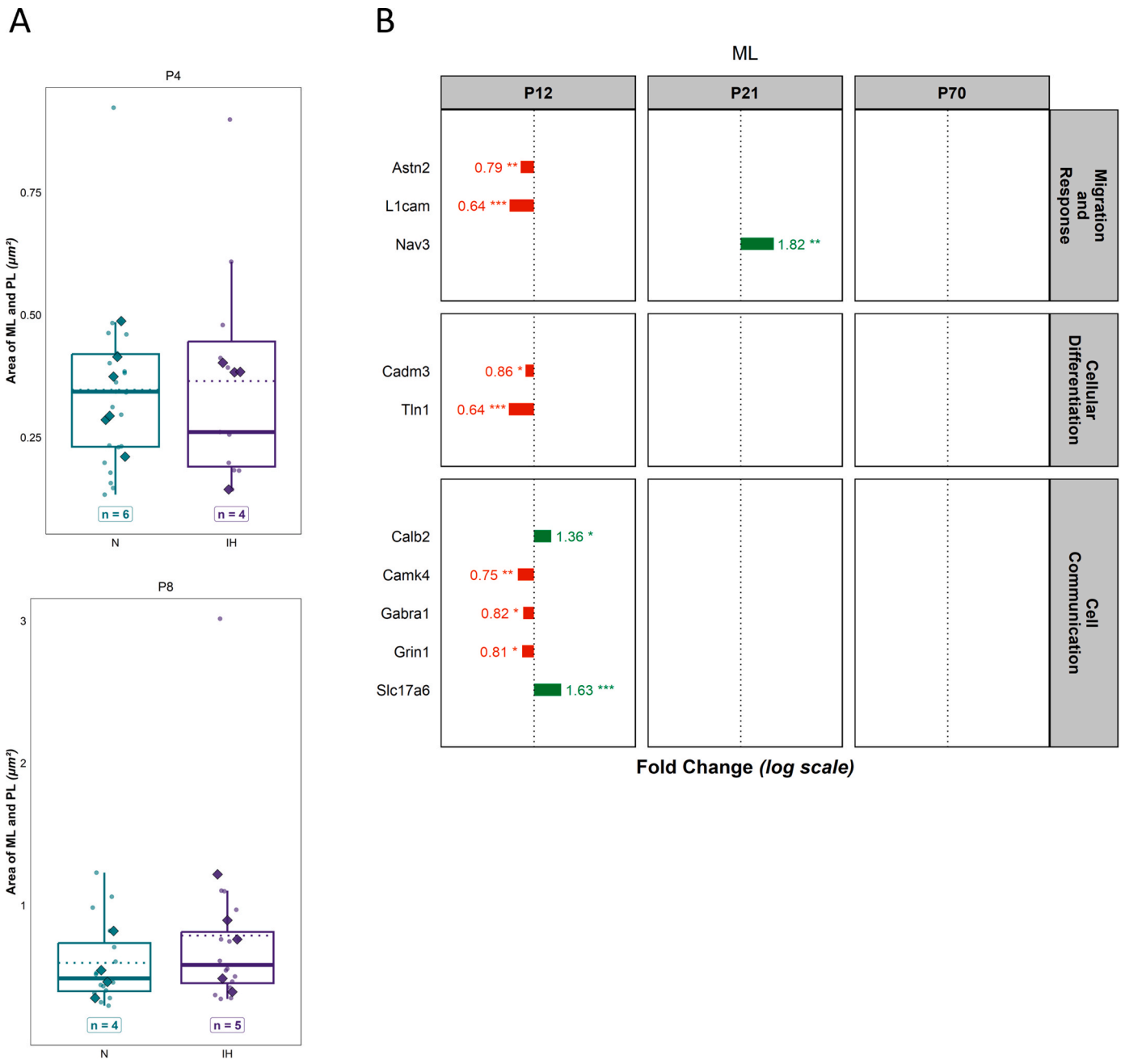

Fig. 7. Effect of IH on the ML and PL. A. Measurement of the area of the ML + PL in control (N) or hypoxic (IH) mice at P4 (upper plot), P8 (bottom plot). Each slice analyzed is represented by a transparent dot, while mouse-averages of slices are represented by diamond shapes. The number of mice (n) present in each experimental group is indicated under each boxplot. **B.** Significant real-time PCR results reflecting the IH-induced regulation of the expression of genes involved in ML differentiation in P12, P21, and P70 mice. Upregulations are represented in green, and downregulations are represented in red. IH: intermittent hypoxia; ML: molecular layer; N: normoxia; Px: postnatal day x. Asterisks indicate the level of statistical significance: one for $p < .05$, two for $p < .01$, and three for $p < .001$. (For interpretation of the references to color in this figure legend, the reader is referred to the Web version of this article.)

No statistically significant difference in the area of the WM was found between IH and N mice at P4 ($t(32) = -1.998$; $p = 0.054$; $Ratio = 0.609$; $CI_{95} = [0.368, 1.01]$) nor P8 ($t(30) = -0.853$; $p = 0.400$; $Ratio = 0.862$; $CI_{95} = [0.604, 1.23]$) (Fig. 10A). The expression of the 30 genes tested is decreased in the WM of P8 and P12 IH mice, except for Akt 1 and Grm3. (Fig. 10B). Interestingly, among these genes, those implicated in the formation of the myelin sheath are simultaneously and strongly downregulated by IH at P12. Moreover, other genes such as Tln1 and Stmn1 present a biphasic expression, with an upregulation at P4 and P70, and a downregulation between P8 and P12 (Fig. 10B).

4. Discussion

In humans, the cerebellum undergoes development from the embryonic stage to beyond the first year of life, rendering it vulnerable to early injury (Volpe, 2009). This vulnerability is particularly pronounced in the case of premature births, where systemic immaturity compounds the risk to the nervous system (Steggerda et al., 2009). Therefore, a participation of the cerebellum in the sequelae observed during AOP (Eichenwald et al., 2016) cannot be excluded. To investigate this hypothesis, we developed a murine model of AOP, based on the IH protocol of Cai et al. (2012). Using this protocol, we showed that IH leads to

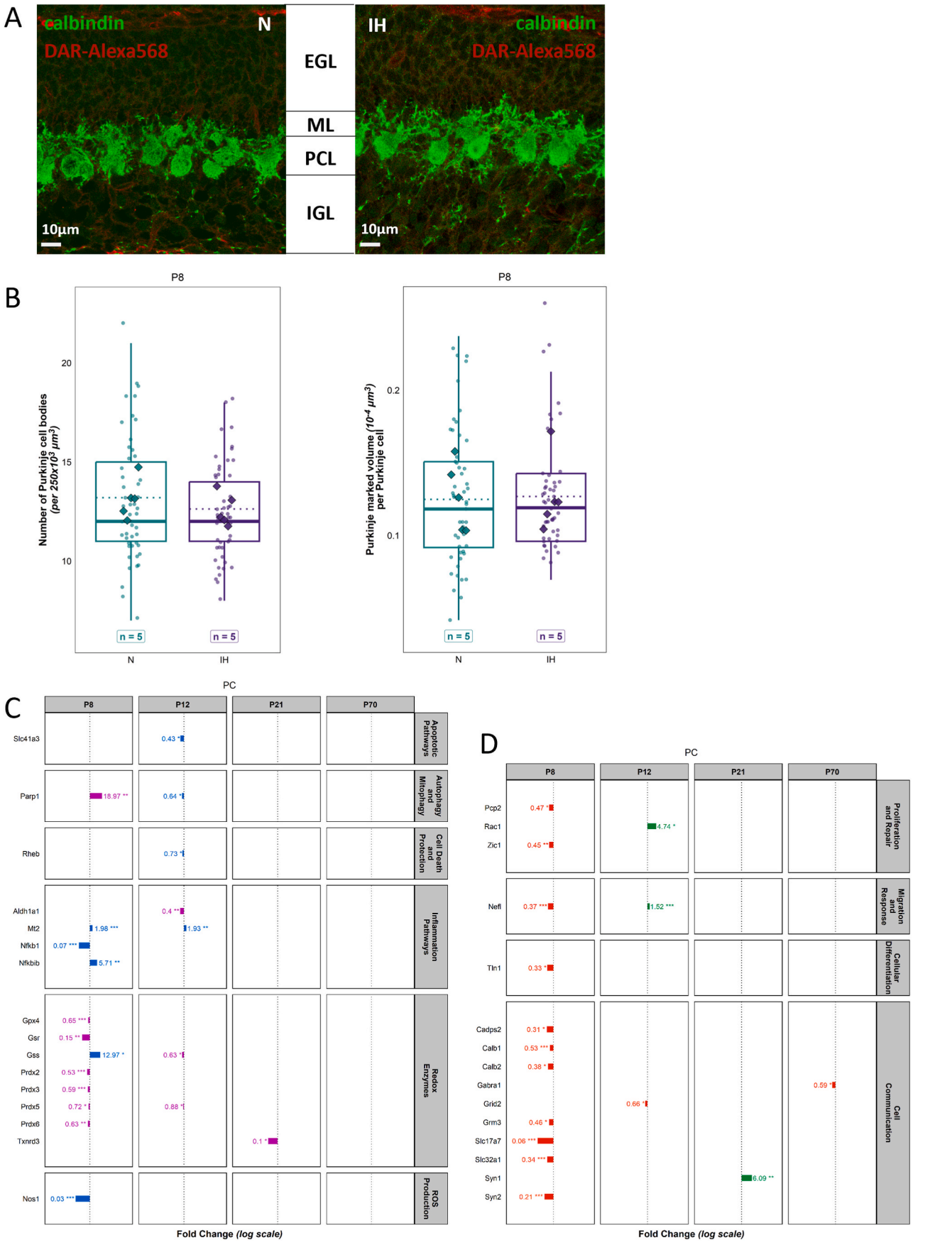

(caption on next page)

Fig. 8. Effect of IH on the morphology and transcriptome of PCs. A. Calbindin labeling (green) of the cerebellar cortex in normoxic (N) or hypoxic (IH) P8 mice. A non-specific labeling of blood vessels with DAR-Alexa568 and the background allow for visualization of the meninges and layer identification. **B.** Measurement of the number of Purkinje cell bodies per frame of 250 × 10^3 μm^3 (left) and of the volume of the calbindin-labeled Purkinje cells (right). Each slice analyzed is represented by a transparent dot, while mouse-averages of slices are represented by diamond shapes. The number of mice (n) present in each experimental group is indicated under the boxplot. **C.** Significant real-time PCR results reflecting the regulation of the expression of genes involved in oxidative stress and cell response after IH in the microdissected PCs of P8, P12, P21, and P70 mice. Deleterious effects (upregulation of pro-oxidative genes or downregulation of anti-oxidative genes) are represented in pink. Positive defense (upregulation of anti-oxidative genes or downregulation of pro-oxidative genes) are represented in blue. **D.** Significant real-time PCR results reflecting the IH-induced regulation of the expression of genes involved in PC differentiation in mice at P8, P12, P21, and P70. Upregulations are represented in green, and downregulations are represented in red. DAR: donkey anti-rabbit; EGL: external granular layer; IGL: internal granular layer; IH: intermittent hypoxia; ML: molecular layer; N: normoxia; PC: Purkinje cell; PCL: Purkinje cell layer; Px: postnatal day x. Asterisks indicate the level of statistical significance: one for $p < .05$, two for $p < .01$, and three for $p < .001$. (For interpretation of the references to color in this figure legend, the reader is referred to the Web version of this article.)

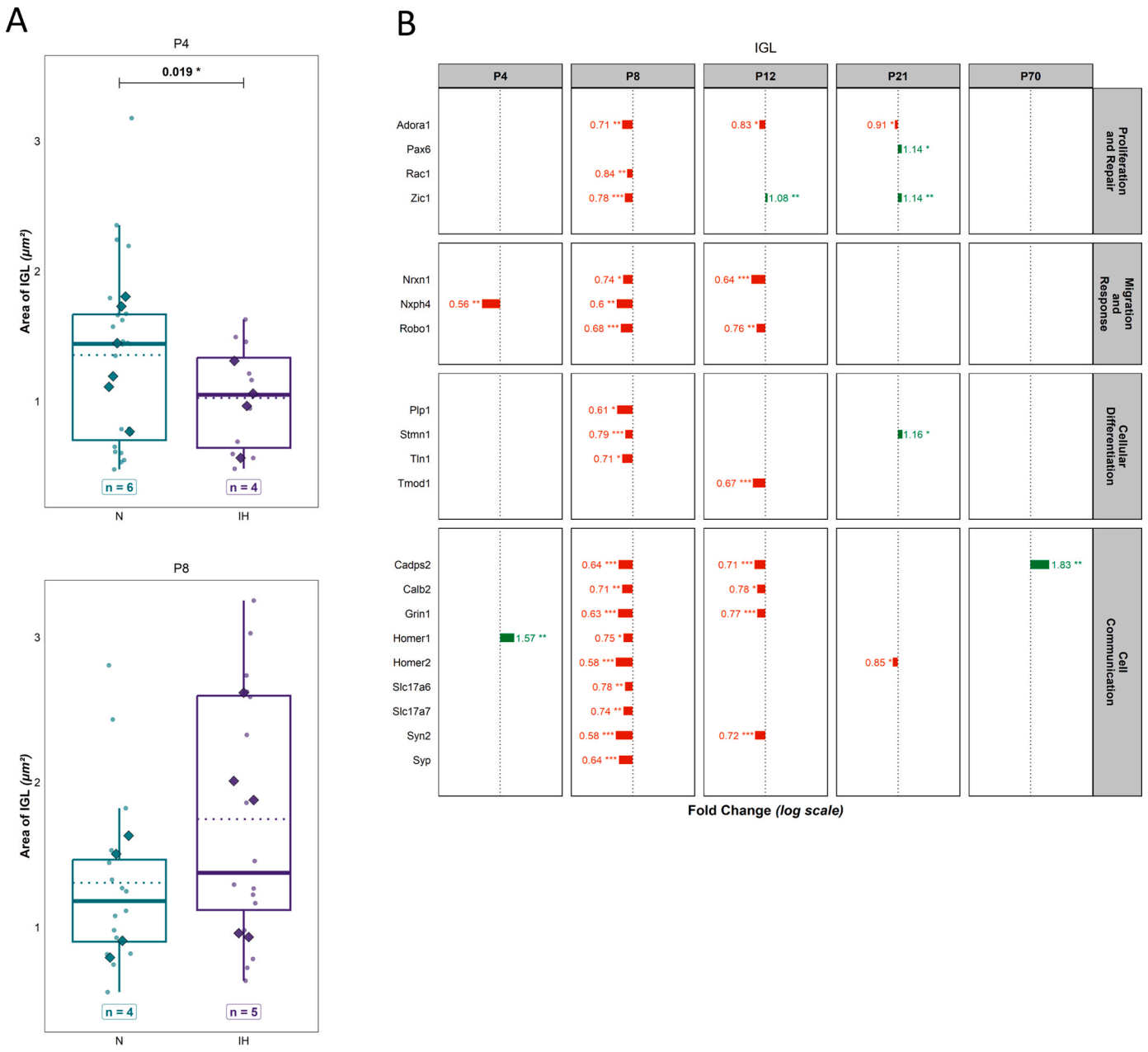

Fig. 9. Effect of IH on the IGL. A. Measurement of the area of the IGL in control (N) or hypoxic (IH) mice at P4 (upper plot), P8 (bottom plot). Each slice analyzed is represented by a transparent dot, while mouse-averages of slices are represented by diamond shapes. The number of mice (n) present in each experimental group is indicated under each boxplot. **B.** Significant real-time PCR results reflecting the IH-induced regulation of the expression of genes involved in IGL differentiation in P4, P8, P12, P21, and P70 mice. Upregulations are represented in green, and downregulations are represented in red. IGL: internal granular layer; IH: intermittent hypoxia; N: normoxia; Px: postnatal day x; WM: white matter. Asterisks indicate the level of statistical significance: one for $p < .05$, two for $p < .01$, and three for $p < .001$. (For interpretation of the references to color in this figure legend, the reader is referred to the Web version of this article.)

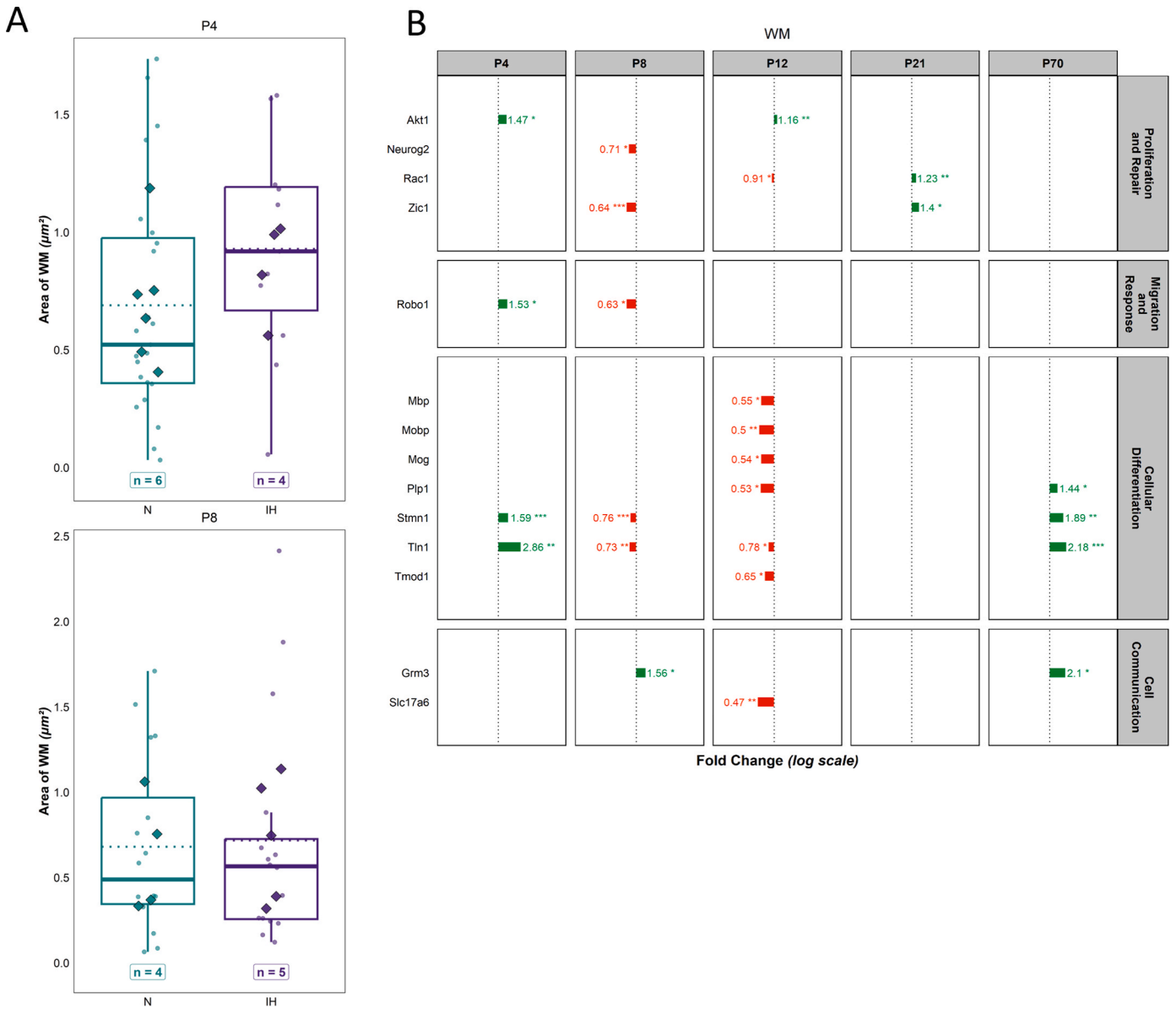

Fig. 10. Effect of IH on the transcriptome of WM cells. A. Measurement of the area of the WM in control (N) or hypoxic (IH) mice at P4 (upper plot), P8 (bottom plot). Each slice analyzed is represented by a transparent dot, while mouse-averages of slices are represented by diamond shapes. The number of mice (n) present in each experimental group is indicated under each boxplot. **B.** Significant real-time PCR results reflecting the regulation of the expression of genes involved in differentiation in the IGL of control (N) or hypoxic (IH) mice at P4, P8, P12, P21, and P70. Upregulations are represented in green, and downregulations are represented in red. N: normoxia; Px: postnatal day x; WM: white matter. Asterisks indicate the level of statistical significance: one for $p < .05$, two for $p < .01$, and three for $p < .001$. (For interpretation of the references to color in this figure legend, the reader is referred to the Web version of this article.)

growth retardation in mice, associated with short and long-term behavioral, and histological alterations (Leroux et al., 2022). To gain a better understanding of the molecular mechanisms underlying these findings, we analyzed the expression of a set of genes related to oxidative stress, cell death, inflammation, and differentiation pathways using real-time PCR. Due to the exploratory nature of this work, we chose to present and discuss all statistically significant results, even if the associated fold changes were small. Indeed, we aim to provide the basis for further proteomic studies, and whether these changes are effectively translated remains to be determined.

We initially confirmed that the cerebellum is sensitive to IH during postnatal development, with evidence of oxidative stress at P4, P8, and P12. Furthermore, we identified P8 as a critical period of vulnerability to IH, where the cerebellar cells' defense against oxidative stress is the most affected. Indeed, we observed the downregulation of genes coding for major antioxidant enzymes, namely, Txnrd1, Sod3, Prdx6, Prdx5 and Cat, which are all involved in neutralizing ROS (Birben et al., 2012). Cerebellar cells appear to initiate compensation mechanisms, beginning at P12, by significantly upregulating Txnrd3 and Sod3. The expression of Hmox1 (heme oxygenase 1), a stress response protein known to respond to hypoxia and exert neuroprotective effects (David et al., 2006; Jazwa and Cuadrado, 2010), was also increased by our IH protocol. However, this antioxidant process seems insufficient since an accumulation of ROS is still present in cultured granule cells and cerebellar explants at P12 post IH (Chiu et al., 2012; Leroux et al., 2022). The protective mechanism appears to continue at P21, with activation of the Txnrd and Gpx pathways, along with increased expression of Idh1. This gene encodes the isocitrate dehydrogenase-1 metabolic enzyme, which produces NADPH (Itsumi et al., 2015), which in turn participates to ROS elimination via reduction reactions. In contrast, Idh1, as well as several other redox enzymes, are downregulated at P70, indicating that the OS state of the cerebellum persists after the end of the protocol, and that IH could

induce long-term alterations. Interestingly, the most marked upregulation in adulthood is Ccs, the gene coding for the copper chaperone of the superoxide dismutase enzyme SOD1 (Furukawa et al., 2004). Thus, a pattern emerges where short-term regulations primarily involve immediate actors in redox reactions, while long-term regulations involve upstream molecules.

Given that several studies have demonstrated that chronic exposure of mice to IH induced caspase-3 activation and increased neuronal apoptosis (Liu et al., 2018; Xu et al., 2004), we analyzed caspase-dependent cell death. At P4, the expression of caspase-3 is not increased, or even detected in IH mice. However, cleaved caspase-3 immunoreactive cells are more abundant in the IGL and the WM of the P4 cerebellum, supporting numerous observations of IH-induced alterations of myelin (Cai et al., 2012; Ferriero, 2001). At P8 and P12, there is no longer a difference in the density of apoptotic cells, despite an increased expression of caspase-3 in IH mice at P12. This belated caspase-3 expression has already been observed in the mouse brain after a continuous perinatal hypoxia (Curristin et al., 2002). However, we did not see any difference in caspase-3 activity at P12 (Leroux et al., 2022), suggesting that this pro-apoptotic process could be compensated by anti-apoptotic factors. One candidate could be Adcyap1 (also known as PACAP, or pituitary adenylate cyclase-activating peptide), which is known to play a neuroprotective role in the cerebellum via the inhibition of caspase-3 activity (Lacaille et al., 2015). Nevertheless, previous works have shown that hypoxia eventually induces a decrease in the volume of the cerebellum in mice at P12, as well as in humans (Leroux et al., 2022; Volpe, 2009). Thus, the loss of cells could be due to a caspase-3-independent apoptosis. Indeed, in hypoxic granule cells, DNA damage caused by the accumulation of ROS can induce apoptosis through the activation of poly ADP-ribose polymerase (PARP) (Chiu et al., 2012). Moreover, it has been demonstrated that Bcl2 can inhibit PARP1 and, as a result, cell death associated with this intracellular pathway (Dutta et al., 2012). Thus, in our model, the under-expression of Bcl2 at P4, P8, and P12 during IH could exacerbate PARP activity and consequently lead to more significant apoptosis. The decrease in the number of granule cells could also be attributed to a defect in cytoprotection. Indeed, we observe a global, albeit slight, decrease in genes that exert a protective effect on cellular components in IH mice at P8. For instance, we observe under-expression of the Sp1 gene, known to be specifically activated by OS and to act as a neuronal survival factor (Ryu et al., 2003).

Another example is Ercc2, which codes for an ATP-dependent DNA helicase, to repair OS-mediated DNA damage. Whether this is part of the metabolic response to save energy after IH or not, the end result is likely an accumulation of DNA damage (Zhao et al., 2021). Thus, several compartments of the cell lack protection when faced with IH-induced OS.

In light of our results, we also hypothesized that cell death could be related to a necrotic phenomenon induced by hypoxia. Indeed, it has been shown that the extracellular spill out of cellular contents after necrosis causes a local inflammation, which could be exacerbated by IH (Xu et al., 2022; Zong and Thompson, 2006). In fact, we observed a strong activation of the anti-inflammatory pathway at P8, which is mostly maintained at P12, suggesting that the cerebellum tries to counteract the pro-inflammatory effect initiated at P4. Indeed, IH induces a downregulation of Nfkb at P8 and a subsequent upregulation of Nfkbib at P12, modifying the expression of two factors known to control inflammation (Dong et al., 2022; Palazzo et al., 2023). Most notably, we highlighted the upregulation of Mt1/2 at P8 and P12, which code for metallothioneins, whose potent anti-inflammatory role may have a cytoprotective effect (Dai et al., 2021; Zhou et al., 2017). Interestingly, the expression of these two genes is significantly decreased at P21, indicating that inflammatory pathways are still implicated after the IH protocol.

A well-known parallel response to IH is a metabolic adaptation, meant to counteract the decrease of mitochondrial production of ATP due to a diminished O_2 availability (Herzig and Shaw, 2018; Peña and Ramirez, 2005). The activation of this mechanism is illustrated by an under-expression of several genes involved in the autophagy/mitophagy pathway, in which dynamin 2, encoded by Dnm2, plays a key role. Indeed, this cytoskeletal protein participates in the mitochondrial fission machinery (Lee et al., 2016), so its downregulation throughout all stages could represent a dual defense mechanism, first by limiting high energy processes in a context of energetic scarcity, while at the same time limiting the ROS-producing mitochondrial pathway.

To determine if some cerebellar cells or processes are more sensitive to IH, we further studied specific molecular pathways, for each developmental stage and cerebellar layer. We showed a downregulation of Zic1, Ccnd1, and Pax6 in the outer EGL at P4, indicating that IH affects the proliferation of GC precursors (Aruga and Millen, 2018; Miyashita et al., 2021; Yeung et al., 2016). This defect results in a significantly smaller EGL in IH mice at P4. Although the under-expression of the proliferative genes is still noticeable at P8, there were no associated histological differences at this stage. Furthermore, our previous results reported an increase in EGL thickness at P12 in IH animals (Leroux et al., 2022). In this latter stage, the proliferation-associated genes are no longer downregulated, and BrDU positive cells are more numerous (Leroux et al., 2022), which could explain how the EGL of IH mice caught up with that of controls at P21. In addition, the downregulation of the guidance-related gene Robo1 at P8 and the upregulation of cadherin 8 at P12 suggest that the thickening of the EGL could be accentuated by a delay in GC migration (Gruner et al., 2019; Taniguchi et al., 2006). However, the most important IH effect on the EGL is visible in the inner premigratory EGL, with marked downregulation of numerous synapse-related genes at P8, such as Grin1, Homer1/2, Slc17a6/7 (Vglut1/2), Syn1, and Syp (Chin et al., 1995; Kao et al., 2017; Parenti et al., 2022). We also found an under-expression of Homer2, which is involved in GC synaptic densities (Shiraishi et al., 2003). In contrast, at P12, some of these genes become upregulated in IH animals, including the GC-enriched calretinin (Calb2) and Homer2, suggesting a delay in the maturation of GC precursors in hypoxic mice (Bearzatto et al., 2006).

Regarding the molecular layer, we refrained from conducting real-time PCR at P4 and P8 due to the high risk of contamination from other cells during microdissection. However, through our immunohistochemical analyses, we found no difference in ML surface area at P4 nor P8. In contrast, we have previously reported that the thickness of the ML (including Purkinje cells) was significantly lower in hypoxic mice at P12 (Leroux et al., 2022). This decrease is associated with the downregulation of migration-associated genes such as Astn2, which should be highly expressed in migrating granule neurons, given the role of astrotactin 2 in glial-guided neuronal migration (Wilson et al., 2010). Likewise, the L1 cell adhesion molecule (L1cam), important for axonal growth and migration (Thelen et al., 2002), is downregulated by our protocol. Similarly, talin 1, which is responsible for neurite outgrowth (Wang et al., 2019), was also downregulated. These dysregulations could imply a deficit in neurite development of ML interneurons and/or Purkinje cells. Interestingly, we also observed changes in several genes implicated in Purkinje cells connectivity, such as Camk4, Grin1, Slc17a6 and Gabra1 (Arsović et al., 2020; Kono et al., 2019; Miyazaki et al., 2003; Nietz et al., 2020). These data suggest that Purkinje innervation by parallel fibers, climbing fibers, and GABAergic interneurons is affected by IH as early as P12, which could explain the locomotor deficits observed after IH during the first postnatal weeks (Leroux et al., 2022). After the end of the protocol, only Nav3, involved in migration, neurite growth, and axon guidance (Powers et al., 2023), is upregulated, suggesting that this molecule may have participated in the compensatory process that allowed the ML thickness of IH mice to catch up to that of controls at P21 (Leroux et al., 2022), and the transcriptomic profile to become similar to control mice by adulthood.

We then focused on Purkinje cells, since they are considered as the integration center of the cerebellum. Although no difference is observed in the phenotype of PCs at P8, our real-time PCR results showed that

these neurons are particularly sensitive to IH at this stage, with a downregulation of both hydrogen peroxide neutralizing enzymes Prdx2, 3, 5, 6, and of the glutathione reducing enzymes, Gpx4 and Gsr (Birben et al., 2012). This defect in the defense against OS is accompanied by a decrease in the expression of genes implicated in the connectivity of Purkinje cells, such as Calb1, Calb2, and Syn2. These downregulations also include VGlut1 (Slc17a7), which represents the hallmark of GC-PC synapses after the first postnatal week. Interestingly, a deficit in these synapses has been shown to impair the correct pruning of CF-PC synapses (van der Heijden et al., 2021). Therefore, the downregulation of Vglut1 at P8 could trigger a compensatory Vglut2 upregulation at P12 in the ML, which could be the premise of the over-innervation of PCs by CFs in adulthood (Leroux et al., 2022). At P8, PCs also show significant downregulation of the PC-specific Pcp2, suggesting an alteration in PC differentiation (Guan et al., 2005). The expression of Cadps2, which codes for the calcium-dependent activator protein for secretion 2, is decreased at this stage too. Interestingly, this factor is the only one to be still regulated in the IGL at P70. Since Cadps2 has been recently shown to participate in the physiopathology of attention-deficit hyperactivity disorder (ADHD) and spatial memory (Duan et al., 2023), it brings to mind the memory deficits found in behavioral experiments in adult mice after IH (Leroux et al., 2022). Finally, the under-expression of Tln1 at P8 may be associated with our previous finding of a lower volume of PC dendritic trees post-IH (Leroux et al., 2022; Wang et al., 2019). At P12, it seems that PCs try to counteract the deleterious effect of IH through a downregulation of the death-promoting Parp1 and Rheb genes (Chiu et al., 2012). Despite this, several mechanisms are triggered in favor of the reported histological abnormalities. Indeed, we observed an increase of the expression of Rac1, which is known to cause defects in cerebellar foliation, ectopic GCs, and altered Bergmann glia morphology (Mulherkar et al., 2014). In addition, the morphogenesis of PCs starts to present some defects, with the upregulation of the neurofilament light chain gene (Nefl). Neurofilaments are cytoskeletal components enriched at PC axonal "torpedoes" or focal swellings, and, while their function is poorly understood, they seem to be a developmental characteristic which peaks at P11 (Ljungberg et al., 2016). This could signify that, during IH, PCs modify their phenotype, and later, their connection profile. However, in the longer term, IH only modifies the expression of a few genes such as Txrnd3, Gabra1, and Syn1 in PCs. As Syn1 is a crucial effector of synaptic plasticity and axonal elongation, whose alteration is a hallmark of neurodevelopmental disorders such as autism and epilepsy (Chin et al., 1995; Kao et al., 2017; Parenti et al., 2022), we can postulate that this regulation is a compensatory mechanism to counteract the early deficits.

Regarding the IGL, we observed a slight decrease in the area between IH and control mice at P4, but no difference at P8. However, at P8, we found an overall downregulation of genes associated with critical neuronal functions, such as the synaptogenic Homer1/2, Syn2, and Syp. Notably, Nrxn1 and/or its ligand Nxph4 were consistently downregulated during the entire IH protocol period. The alteration of this pathway is associated with impaired inhibitory neurotransmission, and a reduced synapse number, which is implicated in motor learning and coordination deficits (Meng et al., 2019). Thus, the dysregulation of this pathway during the IH protocol may condition the behavioral deficits we evidenced in IH mice (Leroux et al., 2022). At P12, most downregulated genes are involved in the synaptic network such as Grin1, Cadps2, and Syn2, indicating that mature GC functions have been impaired by IH. Moreover, we also found a decrease in the expression of factors such as Stathmin (Stmn1) and Robo1, which are implicated in cell motility and guidance (Giampietro et al., 2005; Gruner et al., 2019). This suggests that mature GCs have difficulties finding their proper localization into the IGL, and then fail to establish synapses. The ectopic cells may eventually be eliminated, explaining the thinner IGL observed at P12 (Leroux et al., 2022).

Finally, despite being less studied than the neuronal population, WM and glial cells are conclusively implicated in the physiopathology of AOP. Indeed, periventricular leukomalacia is a common finding in AOP, while the demyelination of both the peripheral and central nervous systems has been associated with IH (Cai et al., 2012; Ferriero, 2001). Interestingly, in the WM, the major differentiation genes implicated in the formation of the myelin sheath, namely Mbp, Mobp, Mog, and Plp1, are simultaneously and strongly downregulated by IH at P12. Although a compensatory increase in the expression of some of these genes appears in adulthood (Stmn1 and Plp1), the volume of myelin sheaths of Purkinje axons was decreased in adult mice after perinatal IH in the cerebellar cortex (Leroux et al., 2022). Moreover, our transcriptomic results indicate that such a defect could also concern mossy and climbing fibers. Finally, the expression of glutamate metabotropic receptor 3 (Grm3), a hallmark of neuroinflammation, was upregulated in the WM, indicating the presence of fibrous astrocytes and suggesting a post-injury reaction after IH that persists into adulthood and could contribute to the behavioral and cognitive impairments observed (Egan et al., 2004; Zinni et al., 2021).

5. Conclusion

In conclusion, our transcriptomic analysis sheds light on the molecular effects of neonatal oxygen deprivation and perinatal intermittent hypoxia on cerebellar development in mice. The cerebellum is shown to be sensitive to neonatal oxygen deprivation, with P8 being the most sensitive stage. The deleterious effects of IH involve a dual mechanism of increased reactive oxygen species production and a failure of the antioxidant defense system. This culminates in the activation of several cell death mechanisms, associated with an alteration in cellular developmental processes, such as proliferation, migration, neurite outgrowth, synaptogenesis, and myelin sheath formation. These molecular dysregulations correlate with histological and behavioral defects observed in AOP, including motor coordination, learning, and behavior impairments. Despite the presence of compensatory mechanisms, the structural modifications caused by IH persist into adulthood, resulting in impaired cerebellar functions.

Ethic approval

All animal experiments were performed according to the protocols approved by the French Ministry of Agriculture and the European Community Council Directive.

Availability of data and materials

The datasets, analyses and code supporting the conclusions of this article are available in the following GitHub repository at https://github.com/ma-riviere/DE-AoP-23, also referenced on Zenodo under: https://doi.org/10.5281/zenodo.8139284.

Funding

Agalic Rodriguez-Duboc was the recipient of a doctoral fellowship from The *Ministère de l'Enseignement Supérieur, de la Recherche et de l'Innovation*. This work was supported by INSERM U1239 and U1245, University of Rouen Normandie, the Normandy Region and the European Union.

CRediT authorship contribution statement

A. Rodriguez-Duboc: Investigation, Methodology, Project administration, Data curation, Formal analysis, Visualization, Illustration, Validation, Writing – original draft, Writing – review & editing. **M. Basille-Dugay:** Supervision, Investigation, Resources, Writing – review & editing. **A. Debonne:** Investigation, Writing – review & editing. **M.-A. Rivière:** Methodology, Software, Data curation, Formal analysis, Visualization, Validation, Writing – review & editing. **D. Vaudry:** Funding

acquisition, Resources, Conceptualization, Writing – review & editing. **D. Burel:** Conceptualization, Methodology, Funding acquisition, Project administration, Supervision, Resources, Writing – original draft, Writing – review & editing.

Declaration of competing interest

The authors declare that they have no known competing financial interests or personal relationships that could have appeared to influence the work reported in this paper.

Data availability

The link of our data is available in the manuscript

Acknowledgments

We would like to thank François Chadelaud and Dr. Sarah Leroux from Rouen University for the development of the hypoxia chamber. We are grateful to Dr. Hélène Lacaille for the development of the oxidative stress panel during her PhD.

Appendix A. Supplementary data

Supplementary data to this article can be found online at https://doi.org/10.1016/j.crneur.2023.100113.

References

Arsović, A., Halbach, M.V., Canet-Pons, J., Esen-Sehir, D., Döring, C., Freudenberg, F., Czechowska, N., Seidel, K., Baader, S.L., Gispert, S., Sen, N.-E., Auburger, G., 2020. Mouse ataxin-2 expansion downregulates CamKII and other calcium signaling factors, impairing granule—purkinje neuron synaptic strength. Int. J. Mol. Sci. 21, 6673. https://doi.org/10.3390/ijms21186673.

Aruga, J., Millen, K.J., 2018. ZIC1 function in normal cerebellar development and human developmental pathology. In: Aruga, J. (Ed.), Zic Family, Advances in Experimental Medicine and Biology. Springer Singapore, Singapore, pp. 249–268. https://doi.org/10.1007/978-981-10-7311-3_13.

Barron, T., Kim, J.H., 2020. Preterm birth impedes structural and functional development of cerebellar Purkinje cells in the developing baboon cerebellum. Brain Sci. 10, 897. https://doi.org/10.3390/brainsci10120897.

Bearzatto, B., Servais, L., Roussel, C., Gall, D., Baba-Aïssa, F., Schurmans, S., de Kerchove d'Exaerde, A., Cheron, G., Schiffmann, S.N., 2006. Targeted calretinin expression in granule cells of calretininnull mice restores normal cerebellar functions. Faseb. J. 20, 380–382. https://doi.org/10.1096/fj.05-3785fje.

Bindea, G., Mlecnik, B., Hackl, H., Charoentong, P., Tosolini, M., Kirilovsky, A., Fridman, W.-H., Pagès, F., Trajanoski, Z., Galon, J., 2009. ClueGO: a Cytoscape plug-in to decipher functionally grouped gene ontology and pathway annotation networks. Bioinformatics 25, 1091–1093. https://doi.org/10.1093/bioinformatics/btp101.

Biran, V., Heine, V.M., Verney, C., Sheldon, R.A., Spadafora, R., Vexler, Z.S., Rowitch, D. H., Ferriero, D.M., 2011. Cerebellar abnormalities following hypoxia alone compared to hypoxic–ischemic forebrain injury in the developing rat brain. Neurobiol. Dis. 41, 138–146. https://doi.org/10.1016/j.nbd.2010.09.001.

Biran, V., Verney, C., Ferriero, D.M., 2012. Perinatal cerebellar injury in human and animal models. Neurol. Res. Int. 2012, 1–9. https://doi.org/10.1155/2012/858929.

Birben, E., Sahiner, U.M., Sackesen, C., Erzurum, S., Kalayci, O., 2012. Oxidative stress and antioxidant defense. World Allergy Organ. J 5, 9–19. https://doi.org/10.1097/WOX.0b013e3182439613.

Brooks, M.E., Kristensen, K., Benthem, K., van, J., Magnusson, A., Berg, C.W., Nielsen, A., Skaug, H.J., Mächler, M., Bolker, B.M., 2017. glmmTMB balances speed and flexibility among packages for zero-inflated generalized linear mixed modeling. R Journal 9, 378. https://doi.org/10.32614/RJ-2017-066.

Bustin, S.A., Benes, V., Garson, J.A., Hellemans, J., Huggett, J., Kubista, M., Mueller, R., Nolan, T., Pfaffl, M.W., Shipley, G.L., Vandesompele, J., Wittwer, C.T., 2009. The MIQE guidelines: minimum information for publication of quantitative real-time PCR experiments. Clin. Chem. 55, 611–622. https://doi.org/10.1373/clinchem.2008.112797.

Cai, J., Tuong, C.M., Zhang, Y., Shields, C.B., Guo, G., Fu, H., Gozal, D., 2012. Mouse intermittent hypoxia mimicking apnoea of prematurity: effects on myelinogenesis and axonal maturation. J. Pathol. 226, 495–508. https://doi.org/10.1002/path.2980.

Chin, L.S., Li, L., Ferreira, A., Kosik, K.S., Greengard, P., 1995. Impairment of axonal development and of synaptogenesis in hippocampal neurons of synapsin I-deficient mice. Proc. Natl. Acad. Sci. USA 92, 9230–9234. https://doi.org/10.1073/pnas.92.20.9230.

Chiu, S.-C., Huang, S.-Y., Tsai, Y.-C., Chen, S.-P., Pang, C.-Y., Lien, C.-F., Lin, Y.-J., Yang, K.-T., 2012. Poly (ADP-ribose) polymerase plays an important role in intermittent hypoxia-induced cell death in rat cerebellar granule cells. J. Biomed. Sci. 19, 29. https://doi.org/10.1186/1423-0127-19-29.

Curristin, S.M., Cao, A., Stewart, W.B., Zhang, H., Madri, J.A., Morrow, J.S., Ment, L.R., 2002. Disrupted synaptic development in the hypoxic newborn brain. Proc. Natl. Acad. Sci. USA 99, 15729–15734. https://doi.org/10.1073/pnas.232568799.

Dai, H., Wang, L., Li, L., Huang, Z., Ye, L., 2021. Metallothionein 1: a new spotlight on inflammatory diseases. Front. Immunol. 12, 739918 https://doi.org/10.3389/fimmu.2021.739918.

Darnall, R.A., Chen, X., Nemani, K.V., Sirieix, C.M., Gimi, B., Knoblach, S., McEntire, B. L., Hunt, C.E., 2017. Early postnatal exposure to intermittent hypoxia in rodents is proinflammatory, impairs white matter integrity, and alters brain metabolism. Pediatr. Res. 82, 164–172. https://doi.org/10.1038/pr.2017.102.

David, J., Boelens, W.C., Grongnet, J., 2006. Up-regulation of heat shock protein HSP 20 in the hippocampus as an early response to hypoxia of the newborn. J. Neurochem. 99, 570–581. https://doi.org/10.1111/j.1471-4159.2006.04071.x.

Doncheva, N.T., Morris, J.H., Gorodkin, J., Jensen, L.J., 2019. Cytoscape StringApp: network analysis and visualization of proteomics data. J. Proteome Res. 18, 623–632. https://doi.org/10.1021/acs.jproteome.8b00702.

Dong, J., Liao, Y., Wu, B., 2022. TAK-242 ameliorates epileptic symptoms in mice by inhibiting the TLR4/NF-κB signaling pathway. Ann. Transl. Med. 10, 795. https://doi.org/10.21037/atm-22-2707. –795.

Duan, K., Chen, J., Calhoun, V.D., Jiang, W., Rootes-Murdy, K., Schoenmacker, G., Silva, R.F., Franke, B., Buitelaar, J.K., Hoogman, M., Oosterlaan, J., Hoekstra, P.J., Heslenfeld, D., Hartman, C.A., Sprooten, E., Arias-Vasquez, A., Turner, J.A., Liu, J., 2023. Genomic patterns linked to gray matter alterations underlying working memory deficits in adults and adolescents with attention-deficit/hyperactivity disorder. Transl. Psychiatry 13, 50. https://doi.org/10.1038/s41398-023-02349-x.

Dutta, C., Day, T., Kopp, N., van Bodegom, D., Davids, M.S., Ryan, J., Bird, L., Kommajosyula, N., Weigert, O., Yoda, A., Fung, H., Brown, J.R., Shapiro, G.I., Letai, A., Weinstock, D.M., 2012. BCL2 suppresses PARP1 function and nonapoptotic cell death. Cancer Res. 72, 4193–4203. https://doi.org/10.1158/0008-5472.CAN-11-4204.

Egan, M.F., Straub, R.E., Goldberg, T.E., Yakub, I., Callicott, J.H., Hariri, A.R., Mattay, V. S., Bertolino, A., Hyde, T.M., Shannon-Weickert, C., Akil, M., Crook, J., Vakkalanka, R.K., Balkissoon, R., Gibbs, R.A., Kleinman, J.E., Weinberger, D.R., 2004. Variation in *GRM3* affects cognition, prefrontal glutamate, and risk for schizophrenia. Proc. Natl. Acad. Sci. USA 101, 12604–12609. https://doi.org/10.1073/pnas.0405077101.

Eichenwald, E.C., , COMMITTEE ON FETUS AND NEWBORN, Watterberg, K.L., Aucott, S., Benitz, W.E., Cummings, J.J., Goldsmith, J., Poindexter, B.B., Puopolo, K., Stewart, D.L., Wang, K.S., 2016. Apnea of prematurity. Pediatrics 137, e20153757. https://doi.org/10.1542/peds.2015-3757.

Ferriero, D.M., 2001. Oxidant mechanisms in neonatal hypoxia-ischemia. Dev. Neurosci. 23, 198–202. https://doi.org/10.1159/000046143.

Furukawa, Y., Torres, A.S., O'Halloran, T.V., 2004. Oxygen-induced maturation of SOD1: a key role for disulfide formation by the copper chaperone CCS. EMBO J. 23, 2872–2881. https://doi.org/10.1038/sj.emboj.7600276.

Giampietro, C., Luzzati, F., Gambarotta, G., Giacobini, P., Boda, E., Fasolo, A., Perroteau, I., 2005. Stathmin expression modulates migratory properties of GN-11 neurons in vitro. Endocrinology 146, 1825–1834. https://doi.org/10.1210/en.2004-0972.

Gruner, H.N., Kim, M., Mastick, G.S., 2019. Robo1 and 2 repellent receptors cooperate to guide facial neuron cell migration and axon projections in the embryonic mouse hindbrain. Neuroscience 402, 116–129. https://doi.org/10.1016/j.neuroscience.2019.01.017.

Gu, Z., Gu, L., Eils, R., Schlesner, M., Brors, B., 2014. *Circlize* implements and enhances circular visualization in R. Bioinformatics 30, 2811–2812. https://doi.org/10.1093/bioinformatics/btu393.

Guan, J., Luo, Y., Denker, B.M., 2005. Purkinje cell protein-2 (Pcp2) stimulates differentiation in PC12 cells by Gβγ-mediated activation of Ras and p38 MAPK. Biochem. J. 392, 389–397. https://doi.org/10.1042/BJ20042102.

Haldipur, P., Millen, K.J., Aldinger, K.A., 2022. Human cerebellar development and transcriptomics: implications for neurodevelopmental disorders. Annu. Rev. Neurosci. 45, 515–531. https://doi.org/10.1146/annurev-neuro-111020-091953.

Hardie, D.G., Ross, F.A., Hawley, S.A., 2012. AMPK: a nutrient and energy sensor that maintains energy homeostasis. Nat. Rev. Mol. Cell Biol. 13, 251–262. https://doi.org/10.1038/nrm3311.

Hartig, F., 2022. DHARMa: Residual Diagnostics for Hierarchical (Multi-level/Mixed) Regression Models (Manual).

Henderson-Smart, D.J., 1981. The effect of gestational age on the incidence and duration of recurrent apnoea in newborn babies. J. Paediatr. Child Health 17, 273–276. https://doi.org/10.1111/j.1440-1754.1981.tb01957.x.

Herzig, S., Shaw, R.J., 2018. AMPK: guardian of metabolism and mitochondrial homeostasis. Nat. Rev. Mol. Cell Biol. 19, 121–135. https://doi.org/10.1038/nrm.2017.95.

Iskusnykh, I.Y., Chizhikov, V.V., 2022. Cerebellar development after preterm birth. Front. Cell Dev. Biol. 10, 1068288 https://doi.org/10.3389/fcell.2022.1068288.

Itsumi, M., Inoue, S., Elia, A.J., Murakami, K., Sasaki, M., Lind, E.F., Brenner, D., Harris, I.S., Chio, I.I.C., Afzal, S., Cairns, R.A., Cescon, D.W., Elford, A.R., Ye, J., Lang, P.A., Li, W.Y., Wakeham, A., Duncan, G.S., Haight, J., You-Ten, A., Snow, B., Yamamoto, K., Ohashi, P.S., Mak, T.W., 2015. Idh1 protects murine hepatocytes from endotoxin-induced oxidative stress by regulating the intracellular NADP+/NADPH ratio. Cell Death Differ. 22, 1837–1845. https://doi.org/10.1038/cdd.2015.38.

Janvier, A., Khairy, M., Kokkotis, A., Cormier, C., Messmer, D., Barrington, K.J., 2004. Apnea is associated with neurodevelopmental impairment in very low birth weight infants. J. Perinatol. 24, 763–768. https://doi.org/10.1038/sj.jp.7211182.

Jazwa, A., Cuadrado, A., 2010. Targeting heme oxygenase-1 for neuroprotection and neuroinflammation in neurodegenerative diseases. Curr. Drug Targets 11, 1517–1531. https://doi.org/10.2174/1389450111009011517.

Kao, H., Ryoo, K., Lin, A., Janoschka, S.R., Augustine, G.J., Porton, B., 2017. Synapsins regulate brain-derived neurotrophic factor-mediated synaptic potentiation and axon elongation by acting on membrane rafts. Eur. J. Neurosci. 45, 1085–1101. https://doi.org/10.1111/ejn.13552.

Kheirandish, L., Gozal, D., Pequignot, J.-M., Pequignot, J., Row, B.W., 2005. Intermittent hypoxia during development induces long-term alterations in spatial working memory, monoamines, and dendritic branching in rat frontal cortex. Pediatr. Res. 58, 594–599. https://doi.org/10.1203/01.pdr.0000176915.19287.e2.

Kono, M., Kakegawa, W., Yoshida, K., Yuzaki, M., 2019. Interneuronal NMDA receptors regulate long-term depression and motor learning in the cerebellum. J. Physiol. 597, 903–920. https://doi.org/10.1113/JP276794.

Lacaille, H., Duterte-Boucher, D., Liot, D., Vaudry, H., Naassila, M., Vaudry, D., 2015. Comparison of the deleterious effects of binge drinking-like alcohol exposure in adolescent and adult mice. J. Neurochem. 132, 629–641. https://doi.org/10.1111/jnc.13020.

Lee, J.E., Westrate, L.M., Wu, H., Page, C., Voeltz, G.K., 2016. Multiple dynamin family members collaborate to drive mitochondrial division. Nature 540, 139–143. https://doi.org/10.1038/nature20555.

Lenth, R.V., 2022. Emmeans: Estimated Marginal Means, Aka Least-Squares Means (Manual).

Leroux, S., Rodriguez-Duboc, A., Arabo, A., Basille-Dugay, M., Vaudry, D., Burel, D., 2022. Intermittent hypoxia in a mouse model of apnea of prematurity leads to a retardation of cerebellar development and long-term functional deficits. Cell Biosci. 12, 148. https://doi.org/10.1186/s13578-022-00869-5.

Liu, F., Liu, T.-W., Kang, J., 2018. The role of NF-κB-mediated JNK pathway in cognitive impairment in a rat model of sleep apnea. J. Thorac. Dis. 10, 6921–6931. https://doi.org/10.21037/jtd.2018.12.05.

Ljungberg, L., Lang-Ouellette, D., Yang, A., Jayabal, S., Quilez, S., Watt, A.J., 2016. Transient developmental Purkinje cell axonal torpedoes in healthy and ataxic mouse cerebellum. Front. Cell. Neurosci. 10 https://doi.org/10.3389/fncel.2016.00248.

Lüdecke, D., Ben-Shachar, M., Patil, I., Waggoner, P., Makowski, D., 2021. Performance: an R package for assessment, comparison and testing of statistical models. J. Open Source Softw. 6, 3139. https://doi.org/10.21105/joss.03139.

Meng, X., McGraw, C.M., Wang, W., Jing, J., Yeh, S.-Y., Wang, L., Lopez, J., Brown, A.M., Lin, T., Chen, W., Xue, M., Sillitoe, R.V., Jiang, X., Zoghbi, H.Y., 2019. Neurexophilin4 is a selectively expressed α-neurexin ligand that modulates specific cerebellar synapses and motor functions. Elife 8, e46773. https://doi.org/10.7554/eLife.46773.

Miyashita, S., Owa, T., Seto, Y., Yamashita, M., Aida, S., Sone, M., Ichijo, K., Nishioka, T., Kaibuchi, K., Kawaguchi, Y., Taya, S., Hoshino, M., 2021. Cyclin D1 controls development of cerebellar granule cell progenitors through phosphorylation and stabilization of ATOH1. EMBO J. 40 https://doi.org/10.15252/embj.2020105712.

Miyazaki, T., Fukaya, M., Shimizu, H., Watanabe, M., 2003. Subtype switching of vesicular glutamate transporters at parallel fibre-Purkinje cell synapses in developing mouse cerebellum: developmental switching of VGluT in parallel fibre. Eur. J. Neurosci. 17, 2563–2572. https://doi.org/10.1046/j.1460-9568.2003.02698.x.

Moriette, G., Lescure, S., El Ayoubi, M., Lopez, E., 2010. Apnées du prématuré : données récentes. Arch. Pediatr. 17, 186–190. https://doi.org/10.1016/j.arcped.2009.09.016.

Mulherkar, S., Uddin, M.D., Couvillon, A.D., Sillitoe, R.V., Tolias, K.F., 2014. The small GTPases RhoA and Rac1 regulate cerebellar development by controlling cell morphogenesis, migration and foliation. Dev. Biol. 394, 39–53. https://doi.org/10.1016/j.ydbio.2014.08.004.

Nietz, A., Krook-Magnuson, C., Gutierrez, H., Klein, J., Sauve, C., Hoff, I., Christenson Wick, Z., Krook-Magnuson, E., 2020. Selective loss of the GABA $_{A\alpha1}$ subunit from Purkinje cells is sufficient to induce a tremor phenotype. J. Neurophysiol. 124, 1183–1197. https://doi.org/10.1152/jn.00100.2020.

Palazzo, I., Kelly, L., Koenig, L., Fischer, A.J., 2023. Patterns of NFkB activation resulting from damage, reactive microglia, cytokines, and growth factors in the mouse retina. Exp. Neurol. 359, 114233 https://doi.org/10.1016/j.expneurol.2022.114233.

Parenti, I., Leitão, E., Kuechler, A., Villard, L., Goizet, C., Courdier, C., Bayat, A., Rossi, A., Julia, S., Bruel, A.-L., Tran Mau-Them, F., Nambot, S., Lehalle, D., Willems, M., Lespinasse, J., Ghoumid, J., Caumes, R., Smol, T., El Chehadeh, S., Schaefer, E., Abi-Warde, M.-T., Keren, B., Afenjar, A., Tabet, A.-C., Levy, J., Maruani, A., Aledo-Serrano, Á., Garming, W., Milleret-Pignot, C., Chassevent, A., Koopmans, M., Verbeek, N.E., Person, R., Belles, R., Bellus, G., Salbert, B.A., Kaiser, F.J., Mazzola, L., Convers, P., Perrin, L., Piton, A., Wiegand, G., Accogli, A., Brancati, F., Benfenati, F., Chatron, N., Lewis-Smith, D., Thomas, R.H., Zara, F., Striano, P., Lesca, G., Depienne, C., 2022. The different clinical facets of SYN1-related neurodevelopmental disorders. Front. Cell Dev. Biol. 10, 1019715 https://doi.org/10.3389/fcell.2022.1019715.

Peña, F., Ramirez, J.-M., 2005. Hypoxia-induced changes in neuronal network properties. Mol. Neurobiol. 32, 251–284. https://doi.org/10.1385/MN:32:3:251.

Pergolizzi, J.V., Fort, P., Miller, T.L., LeQuang, J.A., Raffa, R.B., 2022. The epidemiology of apnoea of prematurity. J. Clin. Pharm. Therapeut. 47, 685–693. https://doi.org/10.1111/jcpt.13587.

Poets, C.F., 2020. Intermittent hypoxia and long-term neurological outcome: how are they related? Semin. Fetal Neonatal Med. 25, 101072 https://doi.org/10.1016/j.siny.2019.101072.

Powers, R.M., Hevner, R.F., Halpain, S., 2023. The Neuron Navigators: structure, function, and evolutionary history. Front. Mol. Neurosci. 15, 1099554 https://doi.org/10.3389/fnmol.2022.1099554.

Prabhakar, N.R., Semenza, G.L., 2012. Adaptive and maladaptive cardiorespiratory responses to continuous and intermittent hypoxia mediated by hypoxia-inducible factors 1 and 2. Physiol. Rev. 92, 967–1003. https://doi.org/10.1152/physrev.00030.2011.

Ryu, H., Lee, J., Zaman, K., Kubilis, J., Ferrante, R.J., Ross, B.D., Neve, R., Ratan, R.R., 2003. Sp1 and Sp3 are oxidative stress-inducible, antideath transcription factors in cortical neurons. J. Neurosci. 23, 3597–3606. https://doi.org/10.1523/JNEUROSCI.23-09-03597.2003.

Sato, A., Sekine, Y., Saruta, C., Nishibe, H., Morita, N., Sato, Y., Sadakata, T., Shinoda, Y., Kojima, T., Furuichi, T., 2008. Cerebellar development transcriptome database (CDT-DB): profiling of spatio-temporal gene expression during the postnatal development of mouse cerebellum. Neural Network. 21, 1056–1069. https://doi.org/10.1016/j.neunet.2008.05.004.

Scheuer, T., Sharkovska, Y., Tarabykin, V., Marggraf, K., Brockmöller, V., Bührer, C., Endesfelder, S., Schmitz, T., 2017. Neonatal hyperoxia perturbs neuronal development in the cerebellum. Mol. Neurobiol. https://doi.org/10.1007/s12035-017-0612-5.

Schindelin, J., Arganda-Carreras, I., Frise, E., Kaynig, V., Longair, M., Pietzsch, T., Preibisch, S., Rueden, C., Saalfeld, S., Schmid, B., Tinevez, J.-Y., White, D.J., Hartenstein, V., Eliceiri, K., Tomancak, P., Cardona, A., 2012. Fiji: an open-source platform for biological-image analysis. Nat. Methods 9, 676–682. https://doi.org/10.1038/nmeth.2019.

Schmidt, B., Roberts, R.S., Anderson, P.J., Asztalos, E.V., Costantini, L., Davis, P.G., Dewey, D., D'Ilario, J., Doyle, L.W., Grunau, R.E., Moddemann, D., Nelson, H., Ohlsson, A., Solimano, A., Tin, W., for the Caffeine for Apnea of Prematurity (CAP) Trial Group, 2017. Academic performance, motor function, and behavior 11 Years after neonatal caffeine citrate therapy for apnea of prematurity: an 11-year follow-up of the CAP randomized clinical trial. JAMA Pediatr. 171, 564. https://doi.org/10.1001/jamapediatrics.2017.0238.

Shannon, P., Markiel, A., Ozier, O., Baliga, N.S., Wang, J.T., Ramage, D., Amin, N., Schwikowski, B., Ideker, T., 2003. Cytoscape: a software environment for integrated models of biomolecular interaction networks. Genome Res. 13, 2498–2504. https://doi.org/10.1101/gr.1239303.

Shiraishi, Y., Mizutani, A., Yuasa, S., Mikoshiba, K., Furuichi, T., 2003. Glutamate-induced declustering of post-synaptic adaptor protein Cupidin (Homer 2/vesl-2) in cultured cerebellar granule cells: glutamate-induced declustering of Cupidin/Homer. J. Neurochem. 87, 364–376. https://doi.org/10.1046/j.1471-4159.2003.02003.x.

Steggerda, S.J., Leijser, L.M., Wiggers-de Bruïne, F.T., van der Grond, J., Walther, F.J., van Wezel-Meijler, G., 2009. Cerebellar injury in preterm infants: incidence and findings on US and MR images. Radiology 252, 190–199. https://doi.org/10.1148/radiol.2521081525.

Szklarczyk, D., Gable, A.L., Nastou, K.C., Lyon, D., Kirsch, R., Pyysalo, S., Doncheva, N. T., Legeay, M., Fang, T., Bork, P., Jensen, L.J., von Mering, C., 2021. The STRING database in 2021: customizable protein–protein networks, and functional characterization of user-uploaded gene/measurement sets. Nucleic Acids Res. 49, D605–D612. https://doi.org/10.1093/nar/gkaa1074.

Taniguchi, H., Kawauchi, D., Nishida, K., Murakami, F., 2006. Classic cadherins regulate tangential migration of precerebellar neurons in the caudal hindbrain. Development 133, 1923–1931. https://doi.org/10.1242/dev.02354.

Thelen, K., Kedar, V., Panicker, A.K., Schmid, R.-S., Midkiff, B.R., Maness, P.F., 2002. The neural cell adhesion molecule L1 potentiates integrin-dependent cell migration to extracellular matrix proteins. J. Neurosci. 22, 4918–4931. https://doi.org/10.1523/JNEUROSCI.22-12-04918.2002.

van der Heijden, M.E., Lackey, E.P., Perez, R., Işleyen, F.S., Brown, A.M., Donofrio, S.G., Lin, T., Zoghbi, H.Y., Sillitoe, R.V., 2021. Maturation of Purkinje cell firing properties relies on neurogenesis of excitatory neurons. Elife 10, e68045. https://doi.org/10.7554/eLife.68045.

Volpe, J.J., 2009. Cerebellum of the premature infant: rapidly developing, vulnerable, clinically important. J. Child Neurol. 24, 1085–1104. https://doi.org/10.1177/0883073809338067.

Wang, Y., Zhang, X., Tian, J., Shan, J., Hu, Y., Zhai, Y., Guo, J., 2019. Talin promotes integrin activation accompanied by generation of tension in talin and an increase in osmotic pressure in neurite outgrowth. Faseb. J. 33, 6311–6326. https://doi.org/10.1096/fj.201801949RR.

Wilson, P.M., Fryer, R.H., Fang, Y., Hatten, M.E., 2010. Astn2, A novel member of the astrotactin gene family, regulates the trafficking of ASTN1 during glial-guided neuronal migration. J. Neurosci. 30, 8529–8540. https://doi.org/10.1523/JNEUROSCI.0032-10.2010.

Wolterink-Donselaar, I.G., Meerding, J.M., Fernandes, C., 2009. A method for gender determination in newborn dark pigmented mice. Lab. Anim 38, 35–38. https://doi.org/10.1038/laban0109-35.

Xu, J., Li, Q., Xu, C.-Y., Mao, S., Jin, J.-J., Gu, W., Shi, Y., Zou, C.-F., Ye, L., 2022. Obstructive sleep apnea aggravates neuroinflammation and pyroptosis in early brain injury following subarachnoid hemorrhage via ASC/HIF-1α pathway. Neural Regen. Res. 17, 2537. https://doi.org/10.4103/1673-5374.339000.

Xu, W., Chi, L., Row, B.W., Xu, R., Ke, Y., Xu, B., Luo, C., Kheirandish, L., Gozal, D., Liu, R., 2004. Increased oxidative stress is associated with chronic intermittent hypoxia-mediated brain cortical neuronal cell apoptosis in a mouse model of sleep apnea. Neuroscience 126, 313–323. https://doi.org/10.1016/j.neuroscience.2004.03.055.

Yeung, J., Ha, T.J., Swanson, D.J., Goldowitz, D., 2016. A novel and multivalent role of Pax6 in cerebellar development. J. Neurosci. 36, 9057–9069. https://doi.org/10.1523/JNEUROSCI.4385-15.2016.

Zhao, W., Liu, Z., Luo, J., Ma, C., Lai, L., Xia, Z., Xu, S., 2021. The roles of PARP-1 and XPD and their potential interplay in repairing bupivacaine-induced neuron oxidative DNA damage. Aging 13, 4274–4290. https://doi.org/10.18632/aging.202390.

Zhou, S., Yin, X., Jin, J., Tan, Y., Conklin, D.J., Xin, Y., Zhang, Z., Sun, W., Cui, T., Cai, J., Zheng, Y., Cai, L., 2017. Intermittent hypoxia-induced cardiomyopathy and its prevention by Nrf 2 and metallothionein. Free Radic. Biol. Med. 112, 224–239. https://doi.org/10.1016/j.freeradbiomed.2017.07.031.

Zimmerman, K.D., Espeland, M.A., Langefeld, C.D., 2021. A practical solution to pseudoreplication bias in single-cell studies. Nat. Commun. 12, 738. https://doi.org/10.1038/s41467-021-21038-1.

Zinni, M., Mairesse, J., Pansiot, J., Fazio, F., Iacovelli, L., Antenucci, N., Orlando, R., Nicoletti, F., Vaiman, D., Baud, O., 2021. mGlu 3 receptor regulates microglial cell reactivity in neonatal rats. J. Neuroinflammation 18, 13. https://doi.org/10.1186/s12974-020-02049-z.

Zong, W.-X., Thompson, C.B., 2006. Necrotic death as a cell fate. Genes Dev. 20, 1–15. https://doi.org/10.1101/gad.1376506.